

22 **Abstract**

23 Landslides present a significant hazard for humans, but continuous landslide
24 monitoring is not yet possible due to their unpredictability. In recent years, numerical
25 simulation and seismic inversion method have been used to provide valuable data
26 for understanding the entire process of landslide movement. However, each method
27 has shortcomings. Dynamic inversion based on long-period seismic signals gives the
28 force-time history of landslide using empirical Green's function, but lack of detailed
29 flowing characteristics of the hazards. Numerical simulation can simulate the entire
30 movement process, but results are strongly influenced by choice of modelling
31 parameters. Therefore, developing a method for combining those two techniques has
32 become a focus for research in recent years. In this study, we develop such a protocol
33 based on analysis of the 2018 Baige landslide in China. Seismic signal inversion
34 results are used to constrain and optimize the numerical simulation. We apply the
35 procedure to the Baige event and, combined with field/geological survey, show it
36 provides a comprehensive and accurate method for dynamic process reconstruction.
37 We found that the Baige landslide was triggered by detachment of the weathered
38 layer, with severe top fault segmentation. The landslide process comprised four
39 stages: initiation, main slip, blocking, and deposition. Multi-method mutual
40 verification effectively reduces the inherent drawbacks of each method, and multi-
41 method joint analysis improves the rationality and reliability of the results. The
42 approach outlined in this study could help better understand the landslide dynamic

43 process.

44 **Keywords:** Landslide processes reconstruction, Seismic signal analysis, Dynamic
45 inversion, Numerical simulation, 2018 “10.10” Baige Landslide.

46

47 **1. Introduction**

48 Landslides present a significant hazard for humans, the number of fatalities resulting from
49 non-seismic landslides between 2004 and 2016 averaged 4,000 per year (Froude and Petley, 2018).

50 However, they cannot be continuously monitored due to their unpredictability and difficulty of
51 detection (Chen et al., 2013; Yamada et al., 2013; Feng et al., 2016; Wang et al., 2020b), and the
52 landslide movement process cannot be fully understood through post-event field investigation and
53 remote sensing alone. Hence, to aid warning and prevention of landslide hazards and reduce
54 associated losses, there is an urgent need to develop alternative methods to enable in-depth
55 investigation of the dynamic characteristics of landslide generation and movement.

56 Landslide movement generates seismic signals that propagate to the surrounding area. The
57 development of environmental seismology and construction of global seismic networks
58 (Dammeier et al., 2016) means the seismic signals generated by landslide movement can be
59 quantitatively recorded by nearby seismic stations (Walter et al., 2012; Yamada et al., 2012; Chen
60 et al., 2013; Yamada et al., 2013). Seismic signals generated by landslides reflect the duration,
61 location, and scale of the event (Kao et al., 2012; Yamada et al., 2012; Chen et al., 2013); seismic
62 signal analysis is increasingly used for landslide hazard monitoring and early warning, but it also
63 offers a research tool for understanding landslide dynamics. The size and location of landslides

64 can be estimated from the amplitude, frequency range, and time-frequency spectrum of the seismic
65 signal (Favreau et al., 2010; Moretti et al., 2012; Moretti et al., 2015), along with timing of the
66 event (Sakals et al., 2011; Zhang et al., 2019), and landslide dynamics (Yamada et al., 2013; Hibert
67 et al., 2015; Jiang et al., 2016). The method of detecting, locating, and identifying landslide events
68 using broadband seismograph records is based on associating seismic signals with landslide
69 characteristics. Some progress has been made in interpreting landslide seismic signals, but signal
70 recognition is often hindered by interference from seismic signals generated by other factors (Feng,
71 2011; Zhao et al., 2015; Fuchs et al., 2018). Several methods have been developed to solve signal
72 noise pollution (Helmstetter and Garambois, 2010; Feng, 2011), but analysis of landslide dynamic
73 characteristics and reconstruction of landslide processes is still subject to errors and inaccuracies.
74 Recently, filtering of seismic signals has been successfully applied to reconstruct dynamic
75 landslide processes, allowing transition stages to be identified that are difficult to derive from field
76 analysis alone (Yan et al., 2020a, 2020b).

77 Combining seismic signal analysis with dynamic inversion can improve the extraction of
78 landslide dynamic characteristics. Landslide dynamic inversion using long-period seismic records
79 based on a single-force source model (Kanamori and Given, 1982; Kanamori et al., 1984;
80 Hasegawa and Kanamori, 1987; Dahlen, 1993; Fukao, 1995) and a static point source assumption
81 has been widely adopted to study landslide kinematics (Allstadt, 2013; Ekström and Stark, 2013;
82 Yamada et al., 2013; Hibert et al., 2014, 2015; Moore et al., 2017; Gualtieri and Ekström, 2018;
83 Li et al., 2019b; Sheng et al., 2020; Zhao et al., 2020). Predictive relationships between the
84 maximum inverted forces and sliding volume can be derived from inverted landslide force histories

85 (Ekström and Stark, 2013; Chao et al., 2016). Landslide basal friction is estimated directly using
86 a block model (Brodsky et al., 2003; Allstadt, 2013; Yamada et al., 2013; Zhao et al., 2015; Yu et
87 al., 2020) or obtained from seismic analysis coupled with numerical simulation (Moretti et al.,
88 2012, 2015; Yamada et al., 2016, 2018). Although numerical simulation of landslide dynamic
89 processes has achieved remarkable results, there are issues with each of the following three main
90 approaches. The continuous medium approach, including smoothed particle hydrodynamics (SPH)
91 (Pastor et al., 2014), material point method (MPM) (Soga et al., 2016), finite element method
92 (FEM) (Muceku et al., 2016; Wang et al., 2020c), finite volume method (FVM) (Pitman et al.,
93 2003), and finite difference method (FDM) (Shen et al., 2020), is not very effective in describing
94 particle separation and internal fracture of rockslides. The discrete element approach utilizes
95 software such as particle flow code (PFC) (Lo et al., 2011; Zhang et al., 2020a) and DEM solutions
96 (EDEM) (Wang et al., 2020c), but a major issue is low computational efficiency. The thin-layer
97 model, it is based on the thin-layer approximation and depth-averaging of the Navier–Stokes
98 equations without viscosity, but a main issue is low computational accuracy (Moretti et al., 2012,
99 2015; Yamada et al., 2016, 2018). MatDEM uses an innovative matrix discrete element method
100 and three-dimensional contact algorithm, which can realize the efficient numerical simulation of
101 millions of particles (Liu et al., 2013, 2017). However, studies utilizing MatDEM mostly
102 determine the correctness of landslide simulation through comparison with post-event landslide
103 characteristics derived from field investigation (Liu et al., 2017), which may not represent dynamic
104 processes. An alternative approach that offers potential is to use seismic signal inversion as the
105 constraint on landslide dynamic process (Yamada et al., 2016, 2018).

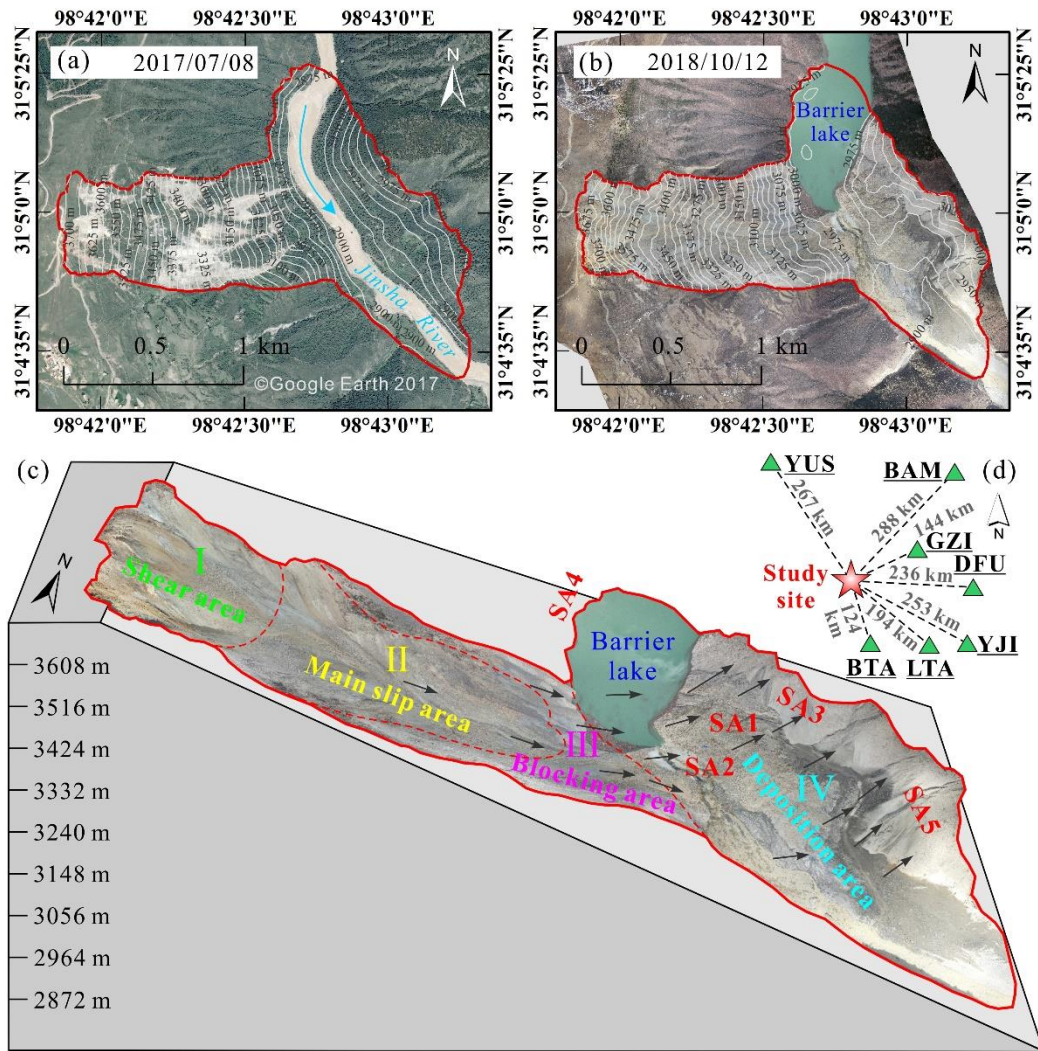
106 In this study, we use long period seismic signal to obtain the dynamic characteristics of Baige
107 landslide, China, which occurred on October 10, 2018 (termed the “10.10” event). By the dynamic
108 inversion results by long period seismic signal which can be used to quality the landslide
109 reconstruction using numerical simulation, and the post-event field investigation and seismic
110 signal analysis, we try to provide an improved characterization of the landslide movement process.

111

112 **2. Study area and data sources**

113 A massive landslide occurred at Baige, on the eastern Qinghai-Tibetan Plateau, China, on
114 October 10, 2018 (Fig. 1). The site is in the Jinsha River suture zone, where the influence of
115 multiple tectonic movements provides a complicated regional tectonic profile; the main fault
116 structures trend NW, within the Jiangda-Bolo-Jinshajiang fault zone (Deng et al., 2019; Fan et al.,
117 2019b; Xu et al., 2018) (Fig. 2). The landslide can be divided into four areas, shear, main slip,
118 blocking, and deposition, with maximum and average thicknesses of 80 and 50 m and thins to the
119 sides (Fig. 1c). We used terrain data from Ouyang et al. (2019), comprising a 10 m resolution pre-
120 landslide Digital Elevation Model (DEM) from 2017, and a 5 m resolution post-slide DEM
121 obtained through Unmanned Aerial Vehicle (UAV) photogrammetry in 2018. Based on DEM
122 differencing, total landslide volume was calculated as c. $1.96 \times 10^7 \text{ m}^3$. The altitude range of the
123 initiation zone is 3523-3730 m. Most of the rock mass that collapsed from the steep back wall
124 accumulated at an elevation of 3100–3300 m, in an area of gentle slope c. 20–25°.

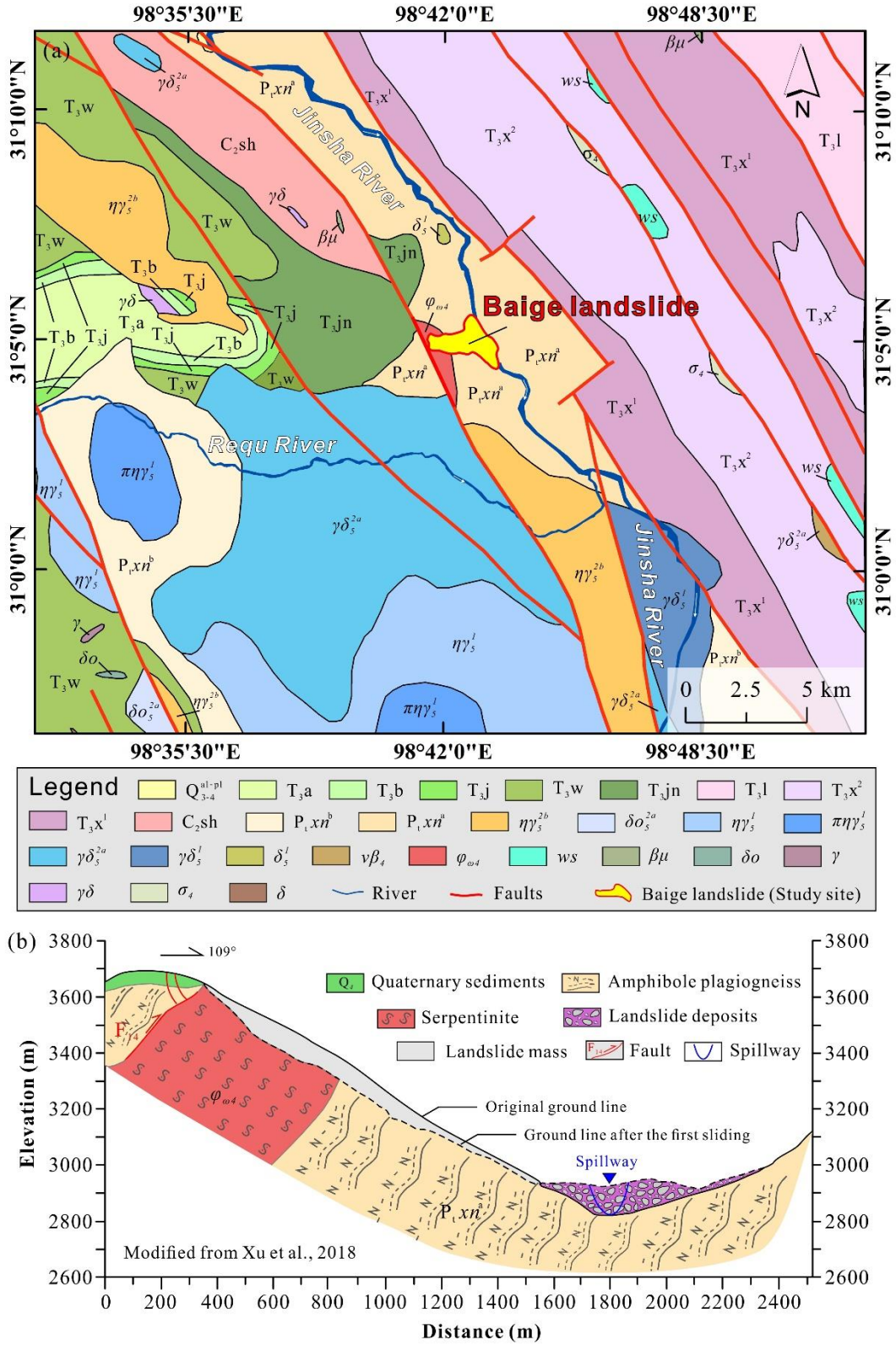
125



126

127 **Fig. 1.** Location of the study area. (a) DOM of Baige landslide 2017; (b) DOM of Baige landslide
 128 after the 2018 event; (c) Schematic cross-section with remote sensing overlay showing key features
 129 of the Baige landslide (SA1 and SA2 is a secondary slip zone formed by small fragments at the
 130 top of the dam body lose stability; SA3 is the left bank of the river, scoured by landslide debris;
 131 SA4 is a small area of the right bank, scoured by landslide debris; SA5 is the downstream left bank,
 132 which is affected by the landslide body mix with the sandblasting water); (d) Location of the Baige
 133 landslide (red star) relative to seismic stations (green triangles) used in the study. The remote
 134 sensing image map data of Fig 1.a. is from the © Google Earth 2017, and the data of Fig 1.b. and
 135 Fig 1.c. are from the authors' own Unmanned Aerial Vehicle (UAV) photography measurements.

136



137

138 **Fig. 2.** Geology of the study area. **(a)** Geological map of the Baige landslide area (Q_{3-4}^{al-pl} :

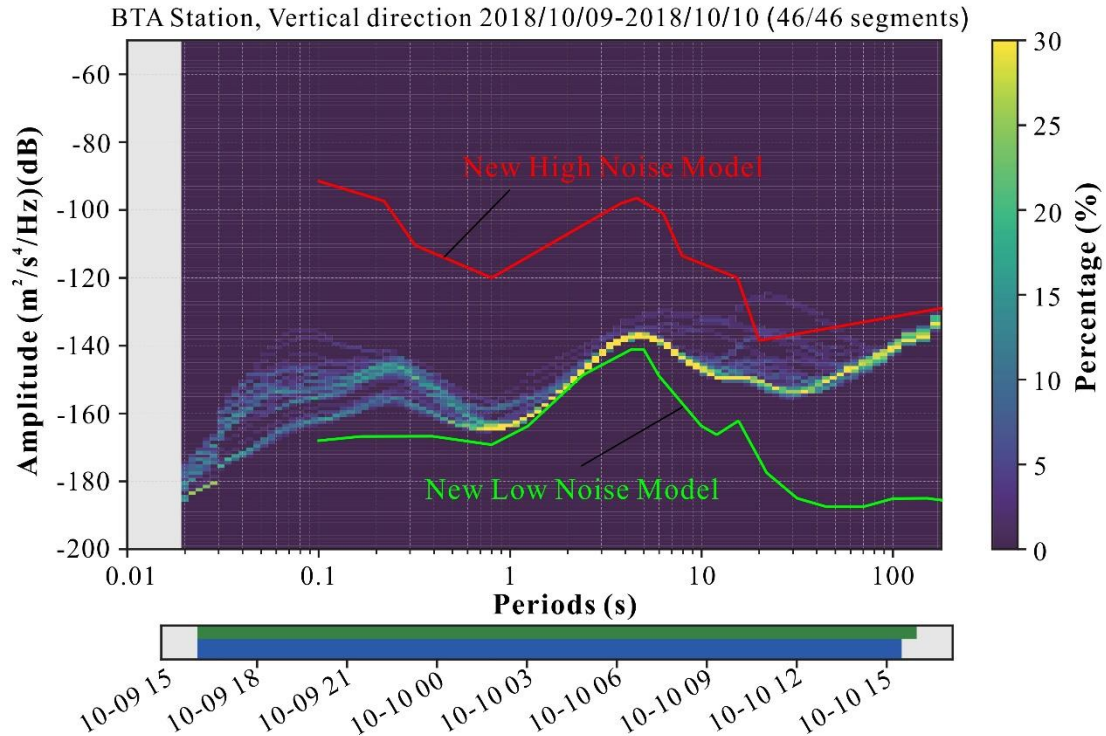
139 Quaternary Holocene Upper Pleistocene; T_3a , T_3b , T_3j , T_3w , T_3jn , T_3l , T_3x^2 , T_3x^1 : Upper
140 Triassic; C_2sh : Upper Carboniferous; P_1xn^b , P_1xn^a : Proterozoic; $n\gamma_5^{2b}$, δo_5^{2a} : Yanshan period;
141 $n\gamma_5^1$, $\pi n\gamma_5^1$, $\gamma\delta_5^{2a}$, $\gamma\delta_5^1$, δ_5^1 : Indosinian; $v\beta_4$, $\varphi\omega_4$, σ_4 : Variscan; ws: Detached block; $\beta\mu$:
142 Diabase-porphyrite; δo : Quartz diorite veins; γ : Granite veins; $\gamma\delta$: Granodiorite dikes; δ : Diorite
143 veins.); **(b)** Cross-section of the landslide showing the geological profile. The geological map data
144 in Figure 2a is from Li et al., 2019a, and the cross-section in Figure 2b is modified from Xu et al.,
145 2018.

146

147 We selected broadband seismic signals from seven seismic stations that are distributed around
148 the landslide with adequate azimuth coverage (Fig. 1d) to carry out the analysis. Landslide force
149 history inversion uses long-period seismic waveforms and thus requires that the ambient noise at
150 periods of tens of seconds should be at a low level in the study area. We used the probabilistic
151 power spectral density (PSD) technique (McNamara and Buland, 2004) to characterize the
152 background seismic noise. As illustrated by the PSD of the vertical component for seismic station
153 BTA (Fig. 3), the main seismic energy is distributed between the new high noise model (NHNM)
154 and the new low noise model (NLNM) (Peterson, 1993), indicating that the study area has a
155 relatively good seismic observation environment.

156

157



158
 159 **Fig. 3.** Probabilistic power spectral density of the vertical component at seismic station BTA.
 160 White lines in the PSD image are NHNM (the upper one) and NLNM (the lower one). Below the
 161 PSD image is a visualization of the data basis for the calculation. The top row shows data fed into
 162 the calculation with green patches representing available data. The bottom row in blue shows the
 163 single PSD measurements that go into the histogram.

164

165 3. Methodology

166 3.1 Seismic data analysis

167 We used short-time Fourier transform (STFT) and PSD to quantitatively analyze the seismic
 168 signals for Baige landslide (Yan et al., 2020a, 2020b). A time-frequency domain transform of the
 169 seismic signal using STFT allowed information on both the time and frequency domain
 170 distributions of the seismic signal to be obtained. The power of each unit of frequency for each
 171 frequency band component that corresponds to a specific moment was estimated based on the PSD
 172 of the seismic signal in the frequency domain.

3.2 Landslide force history inversion

Assuming the landslide source is represented as a series of time-varying forces acting on a static point, synthetic seismograms $u_n(\mathbf{x}, t)$ at the seismic station located at \mathbf{x} can be computed by convolution of force $f_i(\mathbf{x}_0, t_0)$ at \mathbf{x}_0 with nine-component Green's functions $G_{ni}(\mathbf{x}, t; \mathbf{x}_0, t_0)$ (Moretti et al., 2012; Allstadt, 2013; Ekström and Stark, 2013; Yamada et al., 2013; Hibert et al., 2014; Li et al., 2017; Gualtieri and Ekström, 2018),

$$u_n(\mathbf{x}, t) = G_{ni}(\mathbf{x}, t; \mathbf{x}_0, t_0) * f_i(\mathbf{x}_0, t_0) \quad (1)$$

where $*$ denotes convolution and bold type face indicates a vector. The Einstein summation convention is assumed in the equation. The convolution can be rewritten as matrix product,

$$\mathbf{u}_n = [\mathbf{G}_{n1} \quad \mathbf{G}_{n2} \quad \mathbf{G}_{n3}] \begin{bmatrix} \mathbf{f}_1 \\ \mathbf{f}_2 \\ \mathbf{f}_3 \end{bmatrix} \quad (2)$$

Suppose there are N seismic traces,

$$\begin{bmatrix} \mathbf{u}_1 \\ \vdots \\ \mathbf{u}_N \end{bmatrix} = \begin{bmatrix} \mathbf{G}_{11} & \mathbf{G}_{12} & \mathbf{G}_{13} \\ \vdots & \vdots & \vdots \\ \mathbf{G}_{N1} & \mathbf{G}_{N2} & \mathbf{G}_{N3} \end{bmatrix} \begin{bmatrix} \mathbf{f}_1 \\ \mathbf{f}_2 \\ \mathbf{f}_3 \end{bmatrix} \quad (3)$$

Use $\mathbf{u} = \begin{bmatrix} \mathbf{u}_1 \\ \vdots \\ \mathbf{u}_N \end{bmatrix}$, $\mathbf{G} = \begin{bmatrix} \mathbf{G}_{11} & \mathbf{G}_{12} & \mathbf{G}_{13} \\ \vdots & \vdots & \vdots \\ \mathbf{G}_{N1} & \mathbf{G}_{N2} & \mathbf{G}_{N3} \end{bmatrix}$, and $\mathbf{f} = \begin{bmatrix} \mathbf{f}_1 \\ \mathbf{f}_2 \\ \mathbf{f}_3 \end{bmatrix}$, we get the linear forward model

$$\mathbf{u} = \mathbf{G}\mathbf{f} \quad (4)$$

We use \mathbf{u}_o to denote observed seismic records and define the 2-norm of the vector difference between \mathbf{u}_o and \mathbf{u} as an objective function,

$$\mathbf{o} = \|\mathbf{u} - \mathbf{u}_o\|_2 \quad (5)$$

An optimal solution of the forces can be obtained in a least-square sense,

$$\mathbf{f} = (\mathbf{G}^T \mathbf{G})^{-1} \mathbf{G}^T \mathbf{u}_o \quad (6)$$

The landslide force history can be reconstructed by direct deconvolution of the observed seismograms with Green's functions, which can be readily performed in both time and frequency

194 domains (Allstadt, 2013; Yamada et al., 2013; Li et al., 2017). We calculated Green's Function at
195 the landslide location for each seismic station, using a matrix propagation method (Wang, 1999)
196 and a 1-D layered velocity model from Crust1.0 (<https://igppweb.ucsd.edu/~gabi/crust1.html>).

197 Once the landslide force history \mathbf{f} was inverted, based on Newton's third law of motion, the
198 forces acting on the sliding mass could be obtained by multiplying the inverted force history by -
199 1 (Kanamori and Given, 1982; Yamada et al., 2013; Gualtieri and Ekström, 2018). And then the
200 forces acting on the sliding mass can be used to calculate its velocity and displacement
201 distributions for a given mass (Li et al., 2019c; Yu et al., 2020), or to estimate the sliding mass by
202 minimizing discrepancies with independently derived sliding trajectories (Hibert et al., 2014),
203 using the following equations,

$$204 \quad \mathbf{v} = - \int \frac{\mathbf{f}}{m} dt \quad (7)$$

$$205 \quad \mathbf{s} = - \iint \frac{\mathbf{f}}{m} dt \quad (8)$$

206

207 **3.3 Numerical modeling**

208 **3.3.1 Discrete element method**

209 To quantitatively analyze the process of landslide initiation, movement, and accumulation for
210 the "10.10" Baige event, we used MatDEM software, which is based on the matrix discrete element
211 method, to numerically simulate the landslide (Liu et al., 2017). In the discrete element method,
212 particle movement obeys Newton's second law, and particle velocity and displacement are
213 sequentially updated to simulate the dynamic process of the landslide. In MatDEM, the landslide
214 body is formed by the accumulation and cementation of particles endowed with specific

215 mechanical properties, and the contact and interaction of these particles are defined by the linear
 216 elastic bonded model, as shown in Figure 4a. The normal force F_n and tangential force F_s
 217 between particles can be expressed by the following formula:

$$F_n = K_n X_n \quad (9)$$

$$F_s = K_s X_s \quad (10)$$

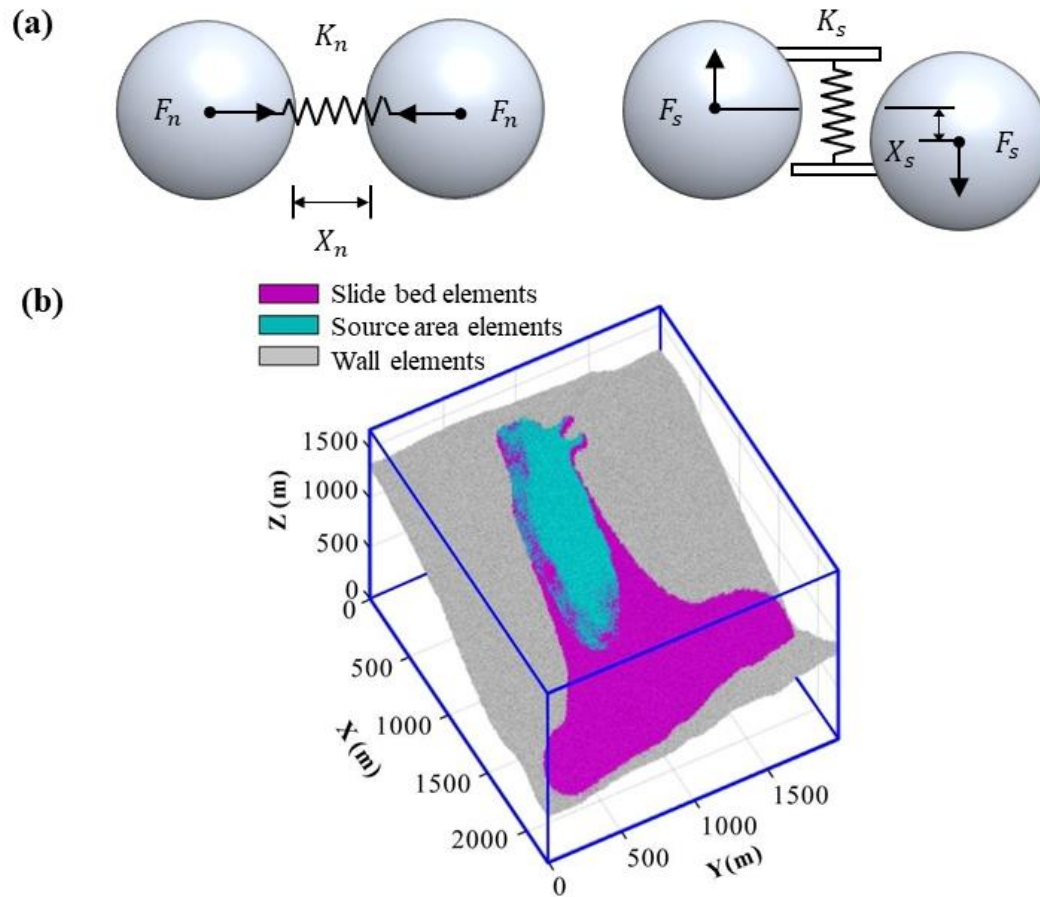
218 where, K_n is the normal stiffness; X_n is the normal relative displacement between two
 219 particles at the contact point; K_s is the tangential stiffness; and X_s is the tangential displacement.

220 In the normal direction, when the displacement between particles X_n exceeds the fracture
 221 displacement X_b the connection between particles is broken and the tension is set as zero. In the
 222 tangential direction, spring failure follows the Mohr-Coulomb criterion, and the tangential bond is
 223 broken when tangential force exceeds maximum shear force F_{smax} , so that only sliding friction
 224 ($-\mu_p F_n$) exists between particles. The maximum normal force F_{nmax} and maximum tangential
 225 force that the cementation between particles F_{smax} can withstand is:

$$F_{nmax} = K_n X_b \quad (11)$$

$$F_{smax} = F_{s0} - \mu_p F_n \quad (12)$$

226 where, F_{s0} is the shear resistance between particles and μ_p is the friction coefficient
 227 between particles.



228

229 **Fig. 4.** Schematics showing properties of landslide particles and discrete element model. (a) Linear
 230 elastic bonded model; (b) Discrete element model of the Baige landslide (Fan et al., 2019a).

231

232 3.3.2 Discrete element model of Baige landslide

233 In MatDEM, the base of the landslide model is constructed of densely packed particles (20 m

234 thick) arranged according to the topography of the slope base. The coordinates of these particles

235 are fixed in the simulation (gray particles in Fig. 4b). The landslide area is constructed by cutting

236 particles accumulated in the cube model box using the pre- and post- landslide topography. Before

237 starting the simulation, gravity is applied to particles in the sliding source area (blue particles in

238 Fig. 4b) and sedimentary layer (20–80 m thick) (purple particles in Fig. 4b); breaking the
239 connection between particles in the source area allows them to slide down under the action of
240 gravity to simulate landslide initiation. We used a simulation block of 2270×1980×1680 m, with
241 582,000 particles comprising 169,000 active cells for simulating landslide movement and 413,000
242 boundary elements to fill the geometry (bottom) and limit the range of activity (side). Average cell
243 size was 5 m and the real-world time 80 s.

244 “We used the dynamic inverted from seismic signals and deposition characteristics as
245 references for the DEM simulation. Initial macro parameter values, such as Young modulus,
246 Poisson’s ratio, were based on results of laboratory tests on Baige landslide materials from Zhou
247 et al. (2019), using the macro and micro conversion formula proposed by Liu et al. (2013) (see
248 Appendix 1 for details), the micro parameters, such as Normal stiffness, Shear stiffness, Breaking
249 displacement, Initial shear resistance, of DEM input can be obtained. As elastic modulus and
250 mechanical properties in laboratory tests are usually higher than those in large-scale rock masses
251 in the field (Darlington et al., 2011; Hencher et al., 2014; Hoek, 2000), Liu et al. (2019) used
252 MatDEM to simulate Xinmo landslide, set Young’s modulus and strength to about 40% of the test
253 value, and obtained appropriate simulation results. Therefore, we used 40% of the test value in our
254 simulation.

255 The second step is to use the geometry of the deposits as a reference to adjusted to obtain
256 reasonable simulation result. For the discrete element method, the geometry of the deposits is
257 affected by the bond strength between particles and the friction coefficient (An et al., 2020), which
258 correspond to the fracture displacement, initial shear force, and friction coefficient between

259 particles in MatDEM. Other parameters, such as normal stiffness and tangential stiffness, remain
260 constant during the simulation. Accuracy of the final landslide accumulation was evaluated by the
261 critical success index (CSI) proposed by Mergili et al. (2017), calculated as:

$$CSI = \frac{TP}{TP + FP + FN} \quad (13)$$

262 where, TP (true positive) is intersection area from both simulation and filed observation, FN
263 (false negative) is the deposition area observed from field that simulation cannot covered, and FP
264 (false positive) is the additional deposition area from simulation where no deposition is observed
265 from site. CSI ranges between 0 and 1, and the higher the value, the more accurate the simulation;
266 when CSI is 1, the simulated accumulation range coincides with the observed. An et al. (2021)
267 conducted 25 simulations by changing the parameters such as static friction coefficient, thermal
268 weakening friction coefficient and normal bond strength. The results showed that only 8 cases had
269 $CSI > 0.6$ and the highest CSI was 0.83. In addition, among the 15 groups of results simulated by
270 Mergili et al. (2017), the maximum CSI is 0.59. Therefore, in this study, the criterion is chosen as
271 $CSI > 0.6$, it can be considered that the simulated accumulation characteristics are basically
272 consistent with the actual situation.

273 The third step is to use the landslide motion velocity and displacement characteristics inverted
274 by the seismic signal as a reference to back-calibrate parameters that affect the kinematic
275 characteristics of the landslide, such as friction and average damping coefficients. A flow chart of
276 the method is shown in Fig. 5, and the final values of the parameters are shown in Table 1.

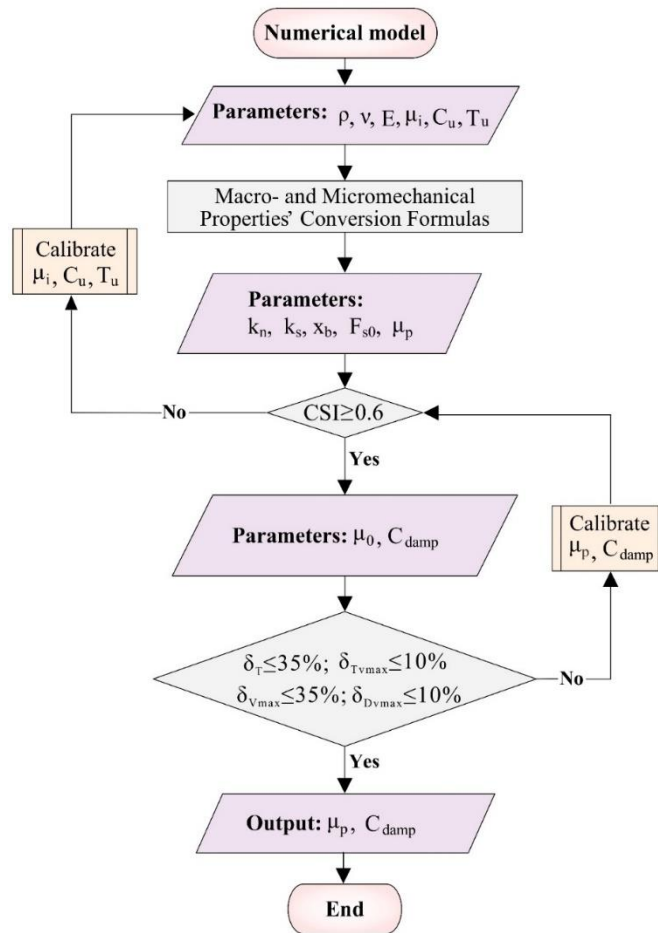
277 The accuracy of simulated and inversed landslide velocity and displacement was
278 preliminarily evaluated by the relative errors of several key points δ . Then, the variance S^2 between

279 the simulated value and the inversion value per second was calculated, and the difference between
 280 the two groups of data in the landslide process was analyzed in detail. Related error δ and
 281 variance S^2 were calculated as:

$$\delta_x = \frac{X_s - X_i}{X_i} \quad (14)$$

$$S^2 = (X_s - X_i)^2 \quad (15)$$

282 where, X_s is the simulated value and X_i the inversed value. X can be replaced by landslide
 283 duration T , peak velocity V_{max} , time when peak velocity achieved T_{Vmax} , and peak displacement
 284 D_{max} .



285
 286 **Fig. 5.** Flowchart of the method of discrete element parameter adjustment based on seismic signal
 287 inversion.

288
289
290

Table 1. Macro- and micromechanical parameters of Baige landslide material used in the discrete element model.

Parameter	Value	Reference
Young modulus E	20 GPa	Laboratory test (Zhou et al. 2019)
Poisson's ratio ν	0.2	Laboratory test (Zhou et al. 2019)
Uniaxial compressive strength C_u	30 MPa	Laboratory test & Calibrated
Uniaxial tensile strength T_u	3 MPa	Laboratory test & Calibrated
Internal friction coefficient μ_i	0.46	Laboratory test & Calibrated
Density ρ	2400 kg/m ³	Zhang et al. (2019)
Normal stiffness k_n	486 GN/m	Calculated (Liu et al., 2013)
Shear stiffness k_s	270 GN/m	Calculated (Liu et al., 2013)
Breaking displacement x_b	1.3 mm	Calculated (Liu et al., 2013)
Initial shear resistance F_{s0}	3.28 GN	Calculated (Liu et al., 2013)
Intergranular friction coefficient μ_p	0.0897	Calculated & Calibrated
Average damping coefficient C_{damp}	1.06×10^5	Calibrated

291

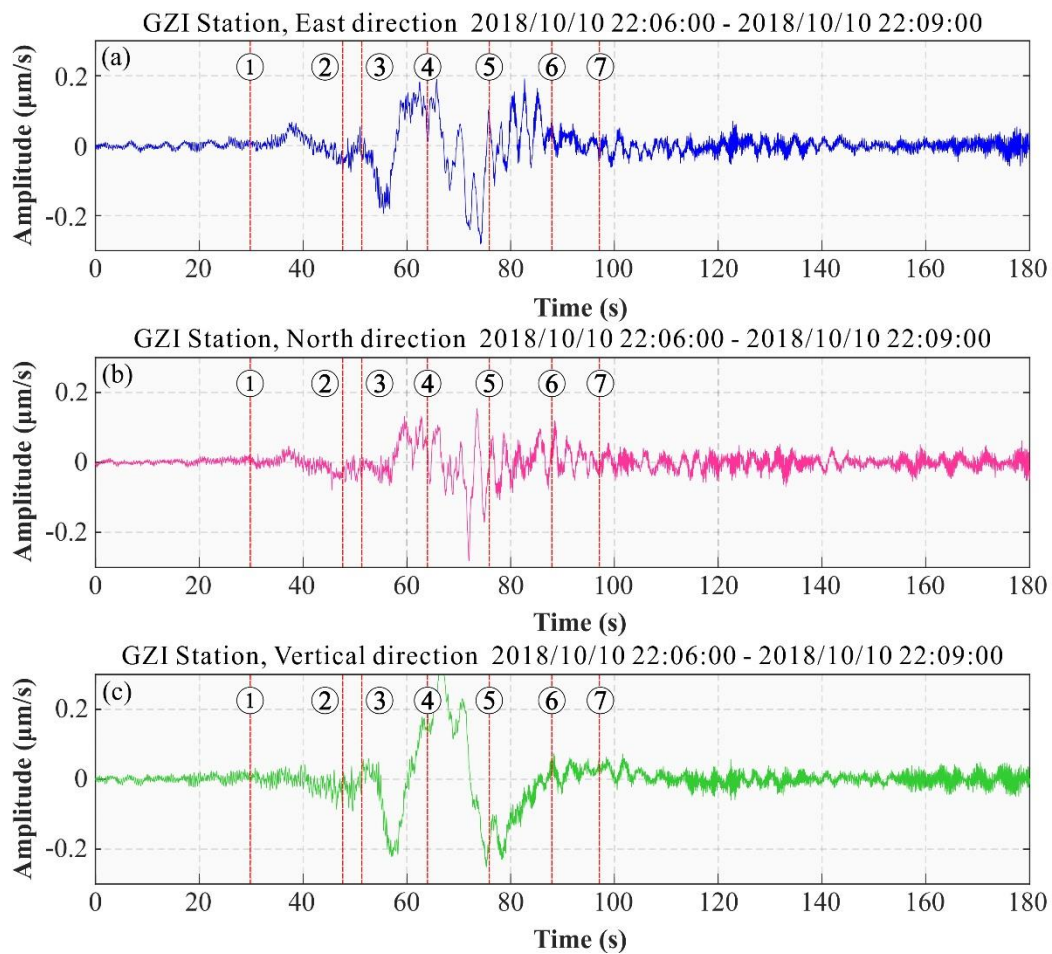
292 **4. Results and analysis**

293 **4.1 Seismic signal analysis**

294 The time-domain velocity curve of the seismic signal generated by the “10.10” Baige
295 landslide is shown in Figure 6. The SNR of the vertical (V) and east (E) components is relative
296 higher, compared with north (N) component, roughly reflecting the main slide direction of
297 landslide is E and N. Post-event geological survey showed sliding was mainly in south-east-to-
298 south, approximately eastwards. The driving force of the landslide is gravity, and the surface on
299 which the mass slides is inclined at about 35°, so acceleration changes in the longitudinal direction
300 are relatively large, and the SNR of the V component of the landslide signal appears high. During

301 the deposition stage, the main horizontal movement direction of landslide body changed from east-
 302 west to north-south, and from north-south limited to east-west limited. The morphology of the
 303 landslide channel means that the landslide stage has a large east-west component and a small north-
 304 south component, and in the deposition stage, it reverses. This feature is consistent with the high
 305 SNR of the N component of the landslide signal and low SNR of the E component.

306



307

308 **Fig. 6.** Time-domain acceleration signal (E \N\V direction) of the seismic generated by the Baige
 309 landslide at GZI seismic station, showing a relative high signal-to-noise ratio visually but different
 310 respectively.

311

312 The sliding distance of the landslide was c. 600 m longitudinally and c. 100 m laterally, while

313 the receiving stations are over 100 km away; as the sliding scale is relatively small relative to the
314 propagation distance, we treated it as a point source. The velocity curve recorded at a seismic
315 station is the velocity of the crustal vibration below the landslide area propagating to the station,
316 and this is roughly determined by velocity and mass of the landslide body. Therefore,
317 characteristics of the landslide downward movement can be obtained by analyzing the velocity
318 curve recorded at seismic stations. The seismic signal from station GZI (Fig. 6) provides an
319 example to show the general seismic characteristics of the “10.10” Baige landslide. The time-
320 domain acceleration curve recorded at GZI determines the start time of the landslide as 22:06 on
321 October 10, 2018 (all times are UTC+8), with a duration of about 76 s between 22:06:39 to
322 22:07:51. Five points of acceleration change are apparent during the landslide process (Fig. 6,
323 Table 2), dividing the event into three phases of acceleration and three of deceleration.

324 Due to seismic wave propagation, the start time determined by the original seismic signal at
325 the station is slightly later than the true time; what’s more, the signal is mixed by longitudinal wave
326 that stack with transverse wave, which makes the ending time picked by seismic signal much latter
327 than the actual time. All these make the time of the landslide derived from the original seismic
328 signal would be lagged and longer, compared to the real time. A more accurate landslide time can
329 be determined by landslide force history inversion as it eliminates the propagation effect. The
330 analysis of the velocity curve recorded at seismic stations is to help understand the overall
331 characteristics of the landslide and help verify the rationality of the subsequent Green's function
332 stress inversion results.

333 **Table 2.** The beginning characteristic stage of the Baige landslide river blocking event picked

334 by seismic signal recorded at GZI station.

Landslide stage						
Start Time	deceleration	acceleration	deceleration	acceleration	deceleration	End Time
22:06:39	22:06:51	22:06:54	22:07:01	22:07:12	22:07:27	22:07:51

335

336 The start and end time of sliding is demarcated on the time spectrum of the seismic curve

337 (Fig. 7); strong energy clusters appear around 22:06:39, the intensity begins to decrease at 22:06:54

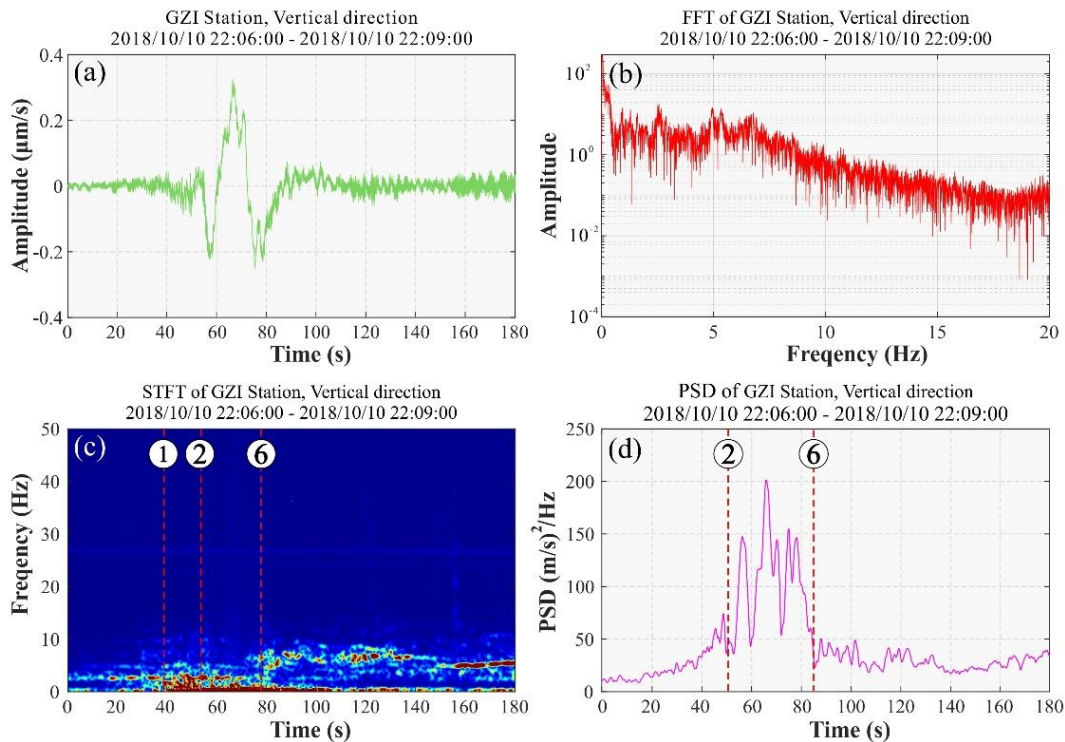
338 (UTC+8), and the frequency band narrows, and the energy disappears at 22:07:27 (UTC+8). The

339 time spectrum shows the landslide was concentrated between 22:06:40–22:07:01. The frequency

340 is concentrated in the 0–1 Hz range, and the low-frequency component has a high SNR (0–0.2 Hz),

341 which is conducive to dynamic inversion.

342



343

344 **Fig. 7.** Seismic signals of the Baige landslide as recorded at seismic station GZI. (a) Vertical

345 seismic signal; (b) Frequency spectrum; (c) Time-frequency spectrum and the key times picked

346 frequency from it, that is, start time, 1st acceleration and 3rd deceleration, from left to right

347 respectively; and **(d)** Power spectral density (PSD) curve and the key times picked from it, that is
348 1st acceleration and 3rd deceleration.

349

350 In Figure 7d, the PSD curve is divided into three stages in the longitudinal direction, with the
351 first and third stages corresponding to slow sliding and the second stage to fast sliding. Comparing
352 with the time domain stages (as in Table 2), the first PSD stage corresponds to the first acceleration
353 and deceleration, the second stage corresponds to the second deceleration, acceleration and third
354 deceleration, and the third stage corresponds to the third deceleration. The PSD curve shows a
355 marked increase in the second stage, indicating rapid downslope sliding, with multiple large
356 fluctuations indicating rapid changes in landslide movement that are characteristic of the sliding
357 stage.

358 According to Yan et al (2021), the frequency of landslide hazard seismic signals is usually
359 low (0~5 Hz), and the morphology in the time-frequency domain and time domain presents single-
360 peak or double-peak characteristics, while the frequency of flood or high-density flow seismic
361 signals is usually high (5~50 Hz), and the morphology in the time-frequency domain and time
362 domain mostly presents the characteristics of flat. Combined with this landslide seismic signal has
363 relatively low frequency (0~1 Hz) and the single-peak feature in time and time-frequency
364 characteristics, apparently different from the spectrum (main frequency :15~30 Hz) of the outburst
365 flood signal triggered by the second landslide on October 12, 2018 (An et al, 2021). So, we think
366 there was no flood discharge during the landslide process.

367 **4.2 Dynamic inversion of landslide**

368 Seismic data were processed using the following procedure before carrying out the landslide
 369 force history inversion. Firstly, they were deconvolved with the instrument response to obtain
 370 displacement; then a 4th-order Butterworth bandpass filter in the frequency band of 0.006–0.2 Hz
 371 was then applied; and finally, the records were resampled at a sampling rate of 5 Hz. The processed
 372 seismic records have a high signal-to-noise ratio (SNR) as shown in Table 3. Sixteen seismic traces
 373 with an SNR larger than 10 dB were selected to carry out the inversion.

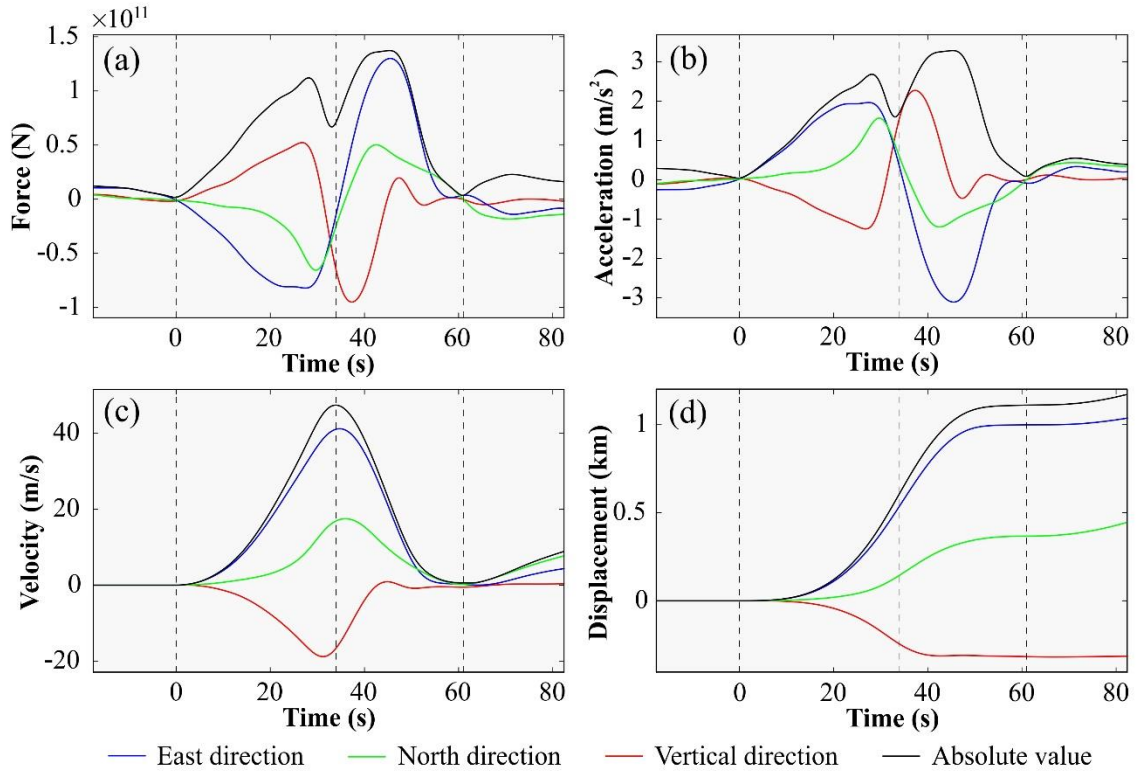
374

375 **Table 3.** SNR of seismic signals used in the inversion and CC and VR of the inversion results

Seismic Station		SNR	CC	VR
BTA	Z	19.19	0.96	0.90
	E	4.28	0.56	0.28
	N	8.45	0.60	0.34
GZI	Z	29.63	0.99	0.99
	E	20.39	0.99	0.98
	N	15.29	0.97	0.94
LTA	Z	24.67	0.99	0.98
	E	7.92	0.86	0.71
	N	15.12	0.97	0.94
DFU	Z	23.60	0.99	0.99
	E	17.58	0.99	0.98
	N	5.92	0.54	0.28
YJI	Z	22.58	0.98	0.97
	E	11.64	0.93	0.85
	N	16.75	0.95	0.90
YUS	Z	18.05	0.94	0.89
	E	19.39	0.98	0.97
	N	18.01	0.98	0.96
BAM	Z	21.48	0.99	0.98
	E	5.86	0.74	0.53
	N	10.91	0.94	0.88

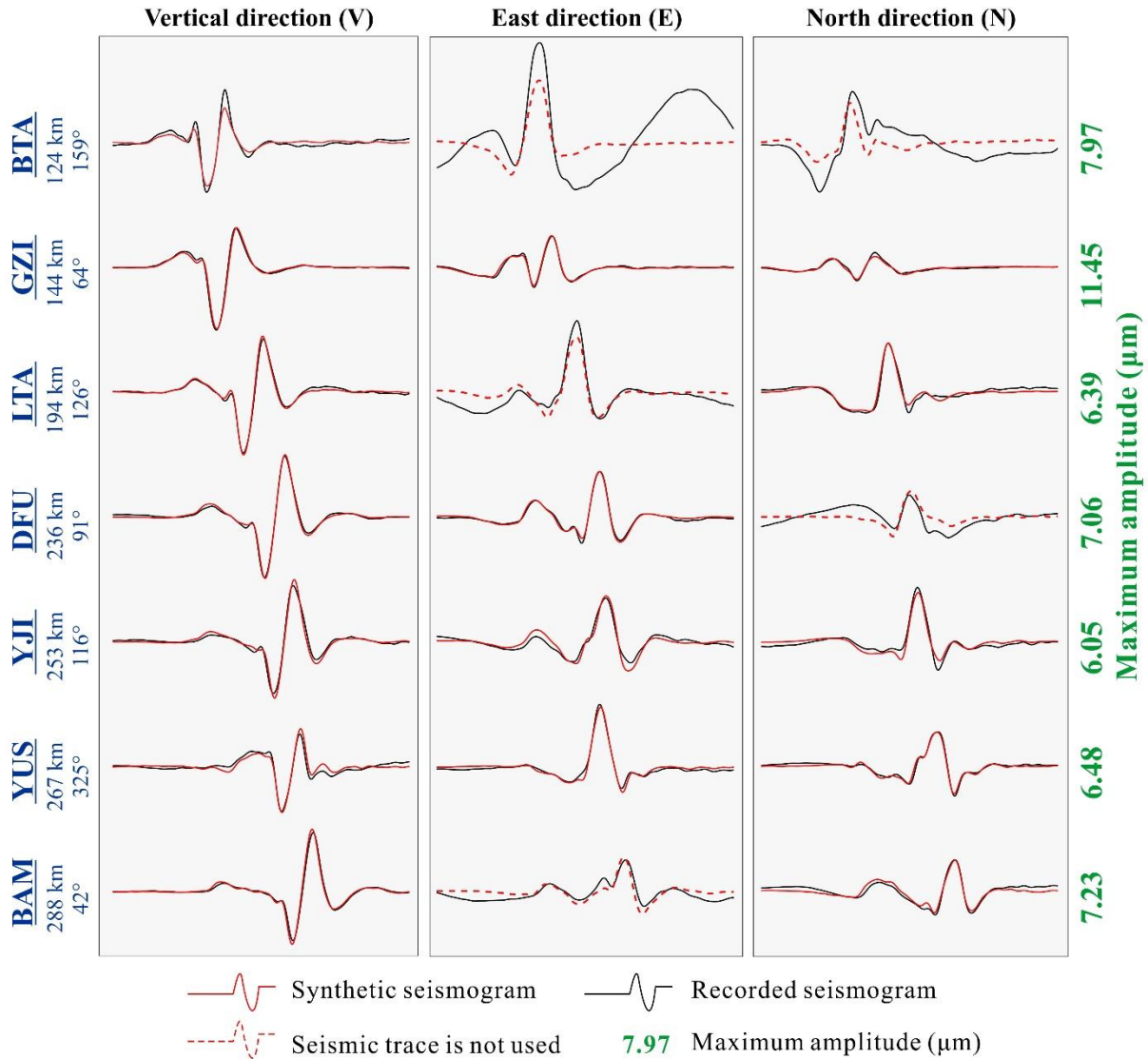
376 The inverted force histories are shown in Fig. 8. The good fit of the synthetic and recorded
 377 seismic waveforms in Fig. 9 and the high cross-correlation (CC) and variance reduction (VR)

378 between synthetic and recorded seismograms provided in Table 3 indicate the high quality of the
 379 inversion results. The inverted forces show landslide initiation at 14:05:37.6, with ~61 s duration
 380 of the main motion.



381 — East direction — North direction — Vertical direction — Absolute value

382 **Fig. 8.** Dynamic inversion used to obtain Baige landslide characteristics. **(a)** Inverted force time
 383 history; **(b)** Estimated acceleration distribution over time; **(c)** Reconstructed velocity distribution
 384 over time from the inverted landslide force time history; **(d)** Reconstructed displacement
 385 distribution over time from the inverted landslide force time history. Corresponding absolute
 386 values are shown as black lines. Dashed vertical black lines marked the landslide start and end
 387 times (the first and third ones) and the time that the sliding mass reached the maximum speed (the
 388 middle one).



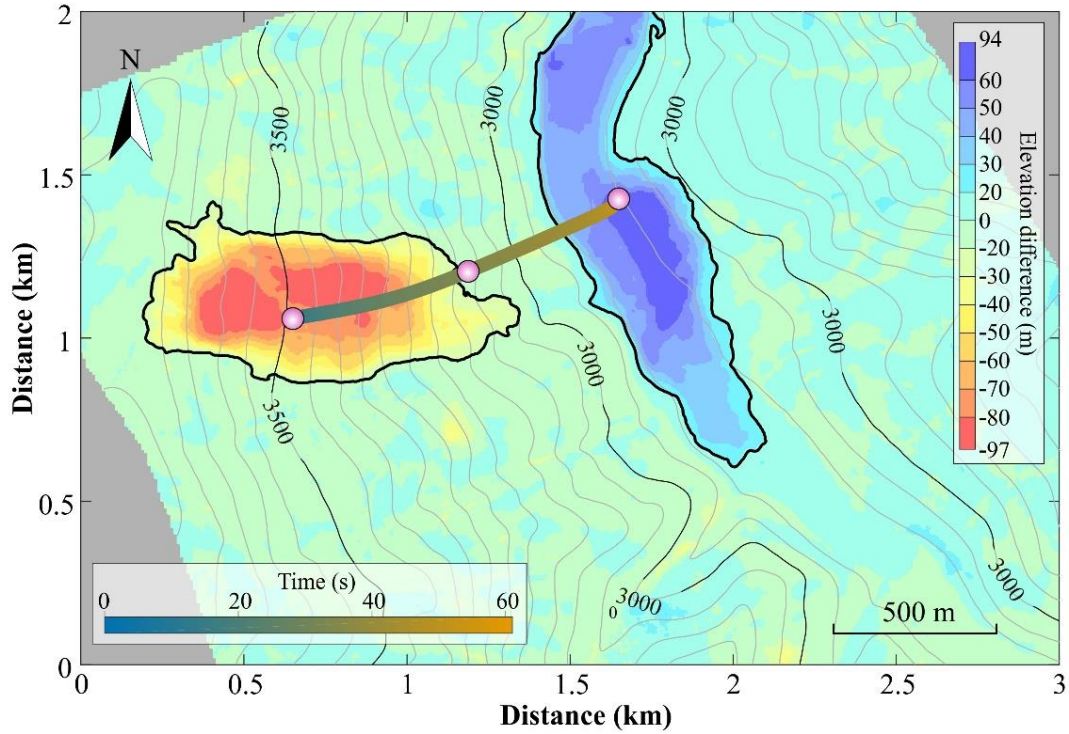
389

390 **Fig. 9.** Seismograms of the Baige landslide. Synthetic (red lines) and recorded (black lines)
 391 seismograms are compared. Red dotted lines indicate that the seismic trace was not used in the
 392 inversion because their SNR is smaller than 10 dB. Station name, distance from study site (km)
 393 and azimuth (degree) are given to the left of each trace (see Fig. 1d for locations), and the
 394 maximum amplitude of the three components is given in μm to the right.

395

396 By comparing the DEMs before and after the event, we determined the mass centers of the
 397 source area and the depositional area and subsequently derived the displacement of the center of
 398 the sliding mass; then, by minimizing the predicted and actual displacements, we estimated the

399 sliding mass as 4.2×10^{10} kg. The recovered sliding trajectory fit well with the observations,
 400 shown in Fig. 10. We used the estimated sliding mass to determine the acceleration and velocity
 401 distributions over time (Figs. 8b to 8d).



402
 403 **Fig. 10.** Reconstructed horizontal trajectory of the Baige landslide from the seismic dynamic
 404 inversion. The base map is the elevation difference derived from DEMs and the reconstructed
 405 trajectory is shown by the colored dots and connecting timeline.

406
 407 The inversion results show two stages of landslide movement, 34 s of acceleration followed
 408 by 27 s of deceleration, which are separated by the vertical dashed black lines in Fig. 8. The sliding
 409 mass reached a maximum velocity of 47.4 m/s at the end of the acceleration stage and then rapidly
 410 decelerated (Fig. 8c). At c. 50 s, the vertical component shows reverse force and velocity,
 411 indicating this was when the main sliding mass traveled over the Jinsha River. The force of the E
 412 and V components increases in a nearly linear manner in the first 26 s, but then decreases rapidly.

413 The reconstructed horizontal trajectory of the landslide (Fig. 10) indicates that the front of the
414 sliding mass ran up the opposite valley wall after it crossed the Jinsha River.

415 **4.3 Numerical modeling results**

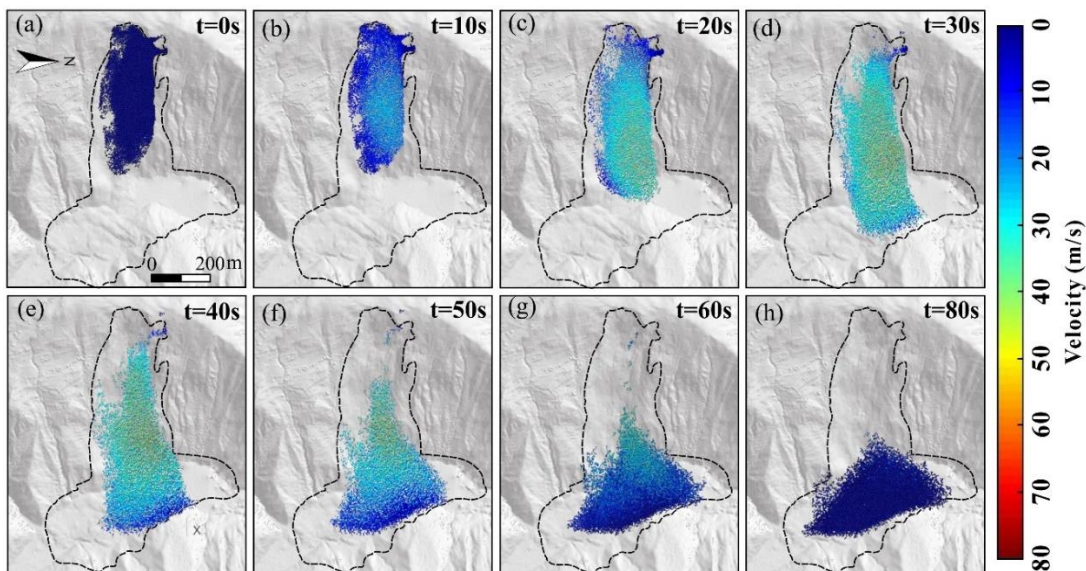
416 According to the results of numerical simulation the movement process of the “10.10” Baige
417 landslide can be divided into three stages: (1) sliding (0–20 s); (2) acceleration when entering the
418 river (20–40 s); and (3) diffusion and accumulation (40–80 s). The velocity distribution through
419 each stage of the simulated landslide is shown in Figure 11.

420 At the start of the simulation, the connection between particles inside and outside the sliding
421 source area was broken simultaneously to initiate the landslide, which then rapidly fell with a
422 constant (gravitational) acceleration. Due to the small particle friction coefficient (0.0897),
423 simulated average velocity and average displacement growth rate are both higher than that
424 determined in the inversion until 18 s, but their variation trends are similar. From the variance
425 results, there is little difference between the simulated and inverted landslide velocity and
426 displacement at this stage, as shown in Fig. 12.

427 In the second stage, the landslide body is moving downwards at a constant acceleration in the
428 simulation, but the inversion shows increased acceleration; so, simulated average velocity and
429 displacement appear to be substantially lower than the inversion. However, the time to reach peak
430 velocity is similar for the simulation (32.8 s) and inversion (32 s). For both velocity and
431 displacement, variance between the inversion and simulation reaches a maximum in this stage,
432 with S^2 of 2.19×10^2 and 2.88×10^4 . At 40 s, the particles at the front edge of the landslide are

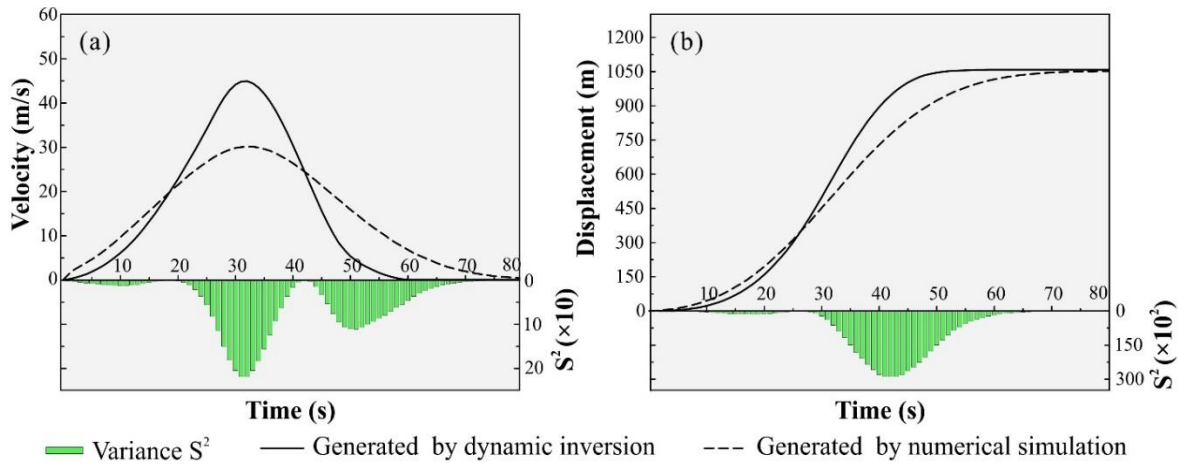
433 stationary due to the obstacle provided by the valley wall/mountain slope on the opposite bank of
434 Jinsha River.

435 In the third stage, from 40 s, particles in the middle and rear of the landslide body continue
436 to move downwards, spreading and accumulating along the river, with a constant deceleration.
437 After 60 s, the simulated average displacement reaches 1020 m and levels off thereafter, which
438 corresponds well with the inversion. Most particles in the landslide body have accumulated and
439 are stationary at this stage, but a few particles on the trailing edge are still moving. By 80 s, the
440 average velocity tends to 0, showing that landslide movement has ended. The variance of velocity
441 residuals has a secondary peak around 50 s, while the displacement variance decreases gradually.
442 Overall, the simulated accumulation area is relatively small compared with that derived from DEM
443 differencing, although the location of maximum thickness corresponds well (Fig. 13b). The CSI is
444 calculated as 0.65, which suggests the simulation is moderately good.



445 **Fig. 11.** Simulated landslide velocity distribution calculated in MatDEM. (a) $t=0$ s; (b) $t=10$ s;
446 (c) $t=20$ s; (d) $t=30$ s; (e) $t=40$ s; (f) $t=50$ s; (g) $t=60$ s; (h) $t=80$ s. The digital terrain model
447 (DTM) data of Fig 11. are from the authors' own UAV photography measurements.
448

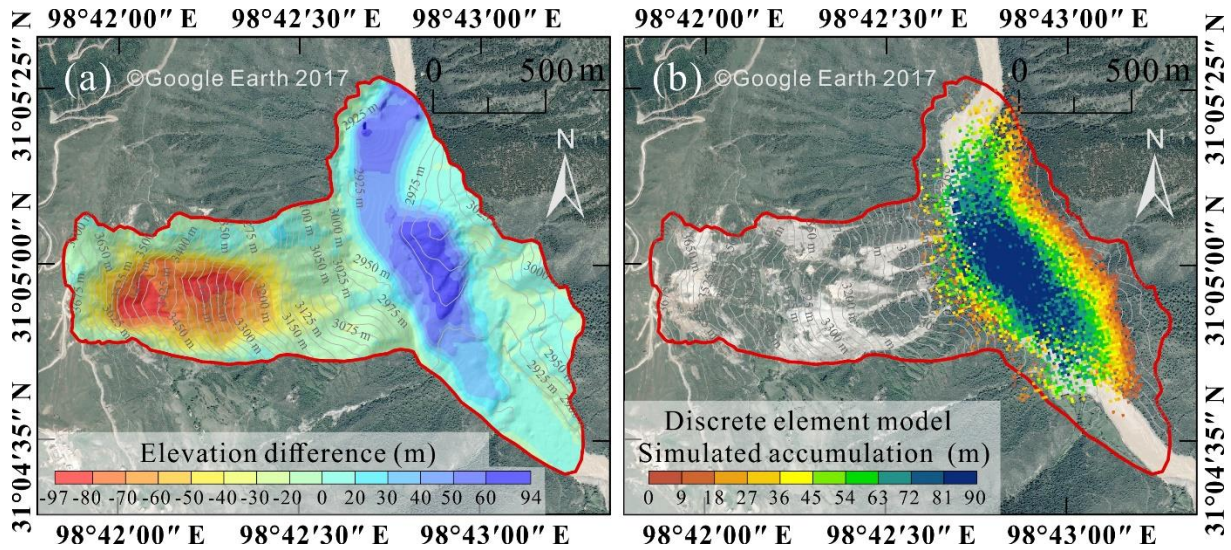
449
450



451

452 **Fig. 12.** Comparison of landslide characteristics simulated using discrete element model with
453 inversion results. (a) Average velocity; (b) Average displacement.

454



455 **Fig. 13.** Comparison of elevation change associated with the Baige landslide. (a) Estimated from
456 pre- and post-failure topography; (b) Calculated using the discrete element model. The remote
457 sensing image map data of Fig 13.a. and b. are from the © Google Earth 2017.
458
459

460 **5. Discussion**

461 **5.1 Field observation and dynamic inversion**

462 Using the empirical relationships of Chao et al. (2016) and Ekström and Stark (2013), the
463 maximum inverted force of 1.37×10^{11} N gives an estimated sliding mass of 5.5×10^{10} kg and

464 7.4×10^{10} kg, respectively, which are about 1.32 and 1.77 times of our estimation of about 4.2×10^{10}
465 kg from landslide force inversion. This is not surprising as we used a different frequency band in
466 our inversion (0.006–0.2 Hz) than the two studies (e.g., Ekström and Stark (2013) used the
467 frequency band 0.0067 – 0.0286 Hz(35–150 s)). Previous work has shown that, for the same event,
468 use of different frequency bands produces landslide force histories of different amplitudes (Hibert
469 et al., 2014; Moore et al., 2017; Zhang et al., 2020b). As a comparison, we performed inversion in
470 the frequency band 0.0067 – 0.0286 Hz, which gave a maximum force of 1.03×10^{11} N and sliding
471 mass estimates of 4.20×10^{10} kg and 5.60×10^{10} kg that are more consistent with our estimation.
472 Since the frequency bands we used are close at the low-frequency end, the kinematic parameters
473 estimated from both inversion results are essentially similar in their characterization of overall
474 landslide motion. We used the frequency band including relatively higher frequency energy (up to
475 0.2 Hz) in the inversion to allow finer scale characteristics of the forces and landslide motion to
476 be analyzed (Zhao et al., 2015), such as the near-linear increase of the vertical component force in
477 the first 26 s and subsequent abrupt decrease.

478 **5.2 Link with numerical modeling**

479 The numerical simulation combining signal inversion and field data more realistically reflects
480 the landslide process than that based on field data alone. Differencing of pre- and post-landslide
481 terrain data is commonly used to calibrate discrete element simulations; however, it is a recognized
482 limitation that this method does not inform on whether the landslide process is correctly modeled.
483 Different combinations of discrete element parameters may produce very similar superposition
484 results even the motion processes differ. In this study, the simulation is calibrated by the

485 accumulation characteristics, and then the landslide movement process is further constrained by
486 the inversion of the seismic signal. The final simulation results produced CSI of 0.65, δT_{vmax} of
487 2.5%, δD_{max} of 0.6%, δT of 33.3%, δV_{max} of 33.3% (δT_{vmax} : error of time corresponds to peak
488 velocity from simulated and inversed; δD_{max} : error of peak displacement from simulated and
489 inversed; δT : error of time of landslide from simulated and inversed; δV_{max} : error of peak velocity
490 from simulated and inversed), indicating they reflect the whole process of movement and
491 accumulation well, overcoming the limitations of traditional methods.

492 Differences in the kinetic characteristics of different landslide phases between the numerical
493 simulation and inversion are highlighted using analysis of variance (Fig. 12). For example, the
494 inversion results simulate the sliding stage (0–20 s) best, the diffusion and deposition stage (40–
495 80 s) second, and the acceleration stage (20–40 s) least. The good simulation of the sliding stage
496 may be due to the fracture zone not yet being completely detached, so landslide movement is
497 dominated by sliding of the whole body, which the theoretical assumption in the inversion
498 approach. In the acceleration stage of large-scale landslides, friction between the sliding rock and
499 soil and the base generates heat, which causes thermal compression and fluidization, leading to
500 soil weakening (Wang et al., 2017, 2018). Reduction in the friction coefficient means the landslide
501 moves faster, however, this factor is not considered in the current inversion model, so it under-
502 estimates peak velocity (Fig. 12). Despite the differences in kinematics, the simulation is
503 essentially consistent with reality in terms of accumulation and movement characteristics.

504 **5.3 Reconstruction of landslide process**

505 The Baige landslide has been the focus of much previous research (Xu et al., 2018; Deng et

506 al., 2019; Fan et al., 2019a; Ouyang et al., 2019; Zhang et al., 2019; Wang et al., 2020a), however,
507 this study is the first analysis that couples seismic signal analysis, dynamic inversion, and
508 numerical simulation. Our approach of multi-method mutual verification effectively reduces the
509 inherent ambiguity of each method, and multi-method analysis improves the rationality and
510 reliability of the results. Based on the characteristics of the “10.10” Baige landslide derived from
511 our seismic signal inversion and discrete element model simulation analysis, we have developed a
512 generic model of landslide dynamics (Figure 14). Our findings show the landslide was triggered
513 by detachment of the weathered layer with severe top fault segmentation and the landslide process
514 comprised four stages: initiation, main slip, blocking, and deposition, as outlined below.

515 1. Initiation stage (Fig. 14a): The fracture zone on the upper part of the first-level platform
516 loses stability and slides down under the action of gravity. Landslide debris is hindered by friction
517 on the surface of the main sliding zone, so the landslide body moves relatively slowly. Increasing
518 debris accumulates on the first-level platform and the lower main sliding area, which increases
519 instability of the weathered layer, and other debris continues to fall downslope. The surface
520 weathering layer of the main sliding area starts to slide, and the landslide body forms after the first
521 fracture in the fracture development zone. Cascading from the initial fracture, continuous
522 fracturing and sliding of the shear zone causes the landslide body to gradually increase; sliding of
523 the top surface of the main sliding zone increases the scale of the landslide body. Downward sliding
524 gradually accelerates as the landslide body increases, but friction in the main sliding area then acts
525 to decelerate the mass; the deceleration process can be seen in the signal recorded at seismic station
526 GZI (Fig. 7). As a result, acceleration increases slowly over c. 10 s; this is evident in both the

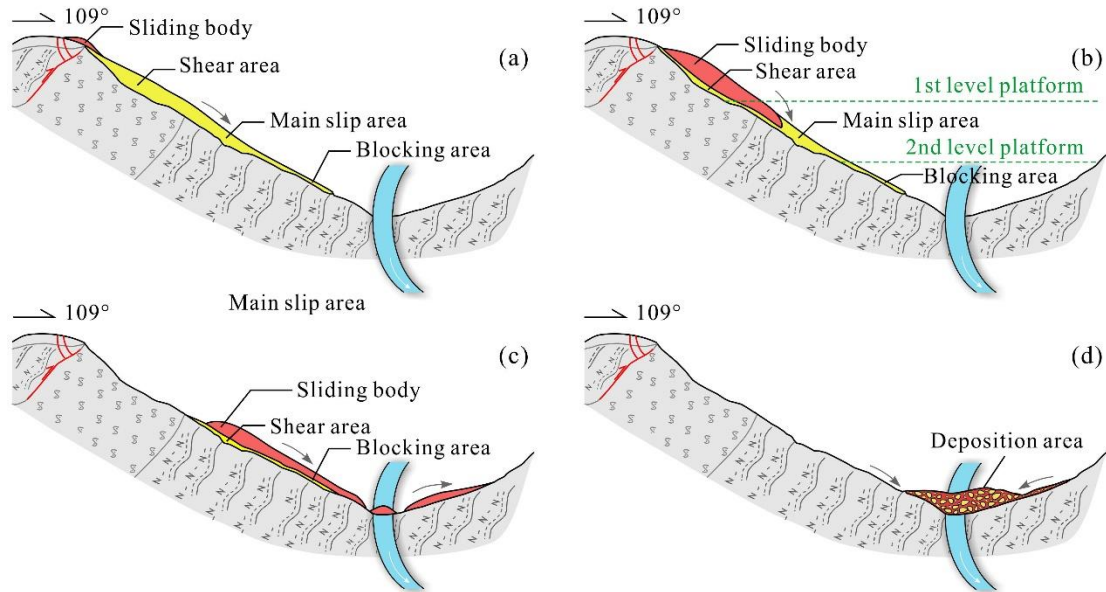
527 inversion and numerical simulation results.

528 2. Main slip stage (Fig. 14b): The main sliding area gradually loses stability and slides rapidly
529 under the control of structural surfaces formed by weathering; the landslide body passes through
530 the main sliding area and enters the wide and gentle second level platform where resistance is
531 relatively high. After crossing the second level platform, the landslide enters the slip resistance
532 zone where the degree of weathering is relatively weak, so the scouring action of the landslide
533 body drives resistance. The effect of both sliding and anti-slip zones on the landslide body is
534 relatively weak and is characterized well by the seismic signal in the time domain and the inverted
535 acceleration curve. The initial sliding stage of the main sliding zone is reflected in the gradually
536 increasing acceleration that peaks when the landslide body reaches the second level platform, and
537 then decreases. When acceleration is approximately zero, the front part of the landslide has entered
538 the river, and velocity of the landslide body peaks; the timing of maximum velocity in the inversion
539 and simulation is consistent, at 32 s and 34 s, respectively (Fig. 12a).

540 3. Blocking stage (Crawling up the opposite valley wall) (Fig. 14c): After passing through the
541 anti-slip area, the landslide detaches at high speed at an altitude of c. 2950 m and loses support of
542 the ground surface. Part of the landslide body accumulates in the river and part hits the opposite
543 (left) bank of the Jinsha River at a high speed and crawls upwards against the valley slope. During
544 the upward movement, landslide debris spreads upstream and downstream, scouring the left bank
545 of the river (SA3 in Fig. 1c) and a small area of the right bank (SA4 in Fig. 1c). Landslide debris
546 reaches a maximum elevation of 3045 m on the opposite slope, then slides downslope under the
547 action of gravity, forming debris strips like the scratches found on the sliding surface. Some debris

548 remains on the relatively gentle slope of the left bank. The main feature of this process is that the
549 action of gravity changes the force of the landslide body from dynamic to resistance; this is well
550 reflected in the time-domain seismic curve and inversion results (Fig. 8), where the acceleration
551 switches rapidly from increasing to decreasing over c. 10 s. As the upward crawling situation was
552 not considered in the model design, the numerical simulation failed to describe the process.

553 4. Deposition stage (Falling back and accumulation) (Fig. 14d): Debris rapidly falls back
554 down under the action of gravity, colliding with debris in the traction area of the river channel and
555 interacting with stream flow to form a jet stream. Some finer particles in the landslide body mix
556 with the sandblasting water to form a water-sand jet that discharges diagonally across the river,
557 toward the downstream left bank (SA5 in Fig. 1c) and upstream right bank (SA4 in Fig. 1c). Most
558 of the detrital material stops moving and is deposited in the river channel, forming a barrier dam
559 that starts to pond water. Under gravity and the action of water flow, small fragments at the top of
560 the dam body lose stability and form a secondary slip zone (SA1 and SA2 in Fig. 1c) that becomes
561 a drainage channel. The acceleration change during this downturn is roughly the same as the
562 change trend of the main sliding phase. Acceleration first gradually increases and then decreases
563 to zero before entering the deceleration phase. The seismic curve in the time domain and the
564 inverted acceleration curve both characterize this process well, and the inversion results give a
565 duration of c. 10 s.



566

567 **Fig. 14.** Schematic diagram of the Baige landslide model. **(a)** Stage 1 –initiation; **(b)** Stage 2 –
 568 main slip; **(c)** Stage 3 – crawling up against the slope (blocking); **(d)** Stage 4 – falling back and
 569 accumulation (deposition).

570

571 **5.4 Research contribution**

572 Post-event geological survey can examine depositional characteristics of the landslide and
 573 weathering and fracture conditions of rocks in the slide source area, which provides some
 574 information for understanding landslide causal processes. The seismic signal provides some
 575 information on landslide evolution, with the low-frequency component reflecting the overall
 576 movement trend of the landslide and the high-frequency component reflecting detailed
 577 characteristics of the movement process. Experienced researchers can reconstruct the landslide
 578 process using a combination of geological survey and seismic signal analysis. However, the
 579 propagation effect of the stratum means that the seismic signal does not completely correspond to
 580 landslide movement and may generate false images, as well as confounding precise determination
 581 of landslide start time and duration.

582 Landslide dynamic inversion based on the long-wavelength information of the seismic signal
 583 eliminates the propagation effect which allows the dynamic parameter curve of the landslide to be
 584 obtained, giving a relatively accurate determination of landslide start and end time and event

585 duration. The dynamic inversion result reflects the change process of the overall movement trend
586 of the landslide (the low-frequency trend) and can be used to verify the results of combined
587 geological survey and seismic signal analysis. The low-frequency (0~0.2 Hz) component of
588 dynamic parameters, as provided by dynamic inversion, can guide the all band frequency motion,
589 concentrating the high frequency (>0.2 Hz) movement, analysis of the landslide process, which
590 helps to reduce ambiguity.

591 The accuracy of numerical simulation results depends on scientific models and accurate
592 parameters. When static parameters such as pre- and post-landslide topography are used to select
593 parameters and constrain results of numerical simulation, there are often multiple solutions. The
594 accuracy of the landslide dynamic with time evolution process will not be determined using only
595 the calibration of the accretion morphology, because different velocities, evolutionary processes
596 may produce similar accretionary landforms (An et al. 2021; Mergili et al. 2017), especially for
597 mega-landslides like Baige, which occur next to deep-incised valleys. Compared with the study of
598 An et al. (2021), which mainly focuses on force time history inversion, we further added the
599 velocity and displacement characteristics retrieved from seismic signals to conduct dynamic
600 quantitative constraints on dynamic parameters and improve the credibility of numerical
601 simulation, so as to carry out efficient simulation of landslide process. The improved simulation
602 allows in-depth analysis of frequency motion characteristics of the landslide, such as speed change,
603 characteristics of each stage, etc. These characteristics can also be used to verify and optimize the
604 landslide process to improve analysis results.

605 Each of the three methods has disadvantages which may lead to errors and ambiguities in
606 analyzing landslides. However, the combined use and mutual verification of the different methods
607 can effectively avoid ambiguity and improve the reasonableness of results.

608

609 **6. Conclusions**

610 In this study, we use on-site geological survey, landslide seismic signal analysis, dynamic
611 inversion, and numerical simulation to provides a comprehensive analysis of “10.10” Baige

612 landslide. We used short-time Fourier transform (STFT) and PSD to analyze the seismic signals
613 for Baige landslide. We then reconstructed the landslide force history by direct deconvolution of
614 the observed seismograms with Green's functions. We then developed a method that use seismic
615 inversion to constrain and calibrate the numerical input parameters using DEM. With the
616 assessment of numerical simulation, the dynamic process of "10.10" Baige landslide was then
617 analysed. Nevertheless, several key issues, such as friction weakening, base entrainment, particle
618 breakage, are not considered in the DEM, which leads the difference between simulation and
619 inversion, should be considered in future research.

620

621 **7. Appendix 1**

622 **Macro and Micro Conversion Formula of Discrete Element Model**

623 There is an analytical solution between the macro and micromechanical parameters of the
624 tightly packed discrete element model, that is, the conversion formula proposed by Liu et al. (2013).
625 For the linear elastic model, there are five micromechanical parameters, that is, the normal stiffness
626 (K_n), shear stiffness (K_s), breaking displacement (X_b), shear resistance (F_{s0}), coefficient of friction
627 (μ_p) can be defined by Young's modulus (E), Poisson's ratio (ν), tensile strength (T_u), compressive
628 strength (C_u) and coefficient of intrinsic friction (μ_i). The conversion formulas are as follows:

629

$$K_n = \frac{E}{\sqrt{3(1-2\nu)(1+\nu)}} \quad (A1)$$

$$K_s = \frac{E(1-4\nu)}{\sqrt{3(1-2\nu)(1+\nu)}} \quad (A2)$$

$$X_b = \frac{2K_n + K_s}{2\sqrt{3}K_n(K_n + K_s)} T_u d \quad (A3)$$

$$F_{s0} = \left(\frac{1}{4} - \frac{\sqrt{3}}{4}\mu_p\right) C_u d \quad (A4)$$

$$\mu_p = \frac{-3\sqrt{3} + \sqrt{3}I}{3 + 3I}, I = [(1 + \mu_i)^{0.5} + \mu_i]^2 \quad (A5)$$

630 where K_n and K_s are the normal and shear stiffness of the particle, respectively; E is Young's
631 modulus; ν is Poisson's ratio; X_b is breaking displacement; T_u is uniaxial tensile strength; d
632 is particle diameter; F_{s0} is initial shear resistance; μ_p is intergranular friction coefficient; C_u is
633 uniaxial compressive strength; μ_i is internal friction coefficient.

634

635 **8. Acknowledgements**

636 This study was financially supported by the National Natural Science Foundation of China
637 (grant nos. 42120104002, 41901008, U21A2008), the Second Tibetan Plateau Scientific
638 Expedition and Research Program (STEP) (grant no. 2019QZKK0906), and the Fundamental
639 Research Funds for the Project of Science & Technology Department of Sichuan Province (grant
640 no. 2020YFH0085).

641 The probabilistic power spectral densities (PSD) are calculated and plotted using ObsPy
642 (<https://docs.obspy.org/>).

643

644 **Data availability**

645 All raw data can be provided by the corresponding authors upon request.

646

647 **Author contributions**

648 The authors of this manuscript entitled "Combining seismic signal dynamic inversion and
649 numerical modeling improves landslide process reconstruction" are Yan Yan, Yifei Cui, Xinghui
650 Huang, Wengang Zhang, Shuyao Yin, Jiaojiao Zhou, Sheng Hu. Yan Yan is the first author, is
651 responsible for most of the work and paper writing in this research. Yifei Cui is the second author
652 and the corresponding author, is responsible for the processing and verification of the article data.
653 Xinghui Huang is the third author and is responsible for the production of the article figures.
654 Wengang Zhang is the fourth author and is responsible for checking the overall logical structure
655 of the article. Shuyao Yin is responsible for the numerical simulations. Jiaojiao Zhou is the seventh

656 author and is responsible for drawing the tables. Sheng Hu is responsible for reviewing and editing
657 the manuscript.

658

659 **Competing interests**

660 The authors declare that they have no conflict of interest.

661

662 **9. References**

- 663 Allstadt, K.: Extracting source characteristics and dynamics of the August 2010 Mount M
664 eager landslide from broadband seismograms, *J. Geophys. Res.-Earth*, 118, 1472–149
665 0, <https://doi.org/10.1002/jgrf.20110>, 2013.
- 666 An, H. C., Ouyang, C. J., Zhao, C., and Zhao, W.: Landslide dynamic process and para
667 meter sensitivity analysis by discrete element method: the case of Turnoff Creek roc
668 k avalanche, *J. Mt. Sci.*, 17, 1581-1595, <https://doi.org/10.1007/s11629020-5993-7>, 20
669 20.
- 670 An, H. C, Ouyang, C. J, Zhou, S.: Dynamic process analysis of the Baige landslide by t
671 he combination of DEM and long-period seismic waves, *Landslides*, 18, 1625-1639,
672 <https://doi.org/10.1007/s10346-020-01595-0>, 2021.
- 673 Brodsky, E. E., Gordeev, E., and Kanamori, H.: Landslide basal friction as measured by
674 seismic waves, *Geophys. Res. Lett.*, 30, 2236, <https://doi.org/10.1029/2003GL018485>,
675 2003.
- 676 Chao, W. A., Zhao, L., Chen, S. C., Wu, Y. M., Chen, C. H., and Huang, H. H.: Seis
677 mology-based early identification of dam-formation landquake events, *Sci. Rep.*, 6, 1
678 9259, <https://doi.org/10.1038/srep19259>, 2016.
- 679 Chao, W. A., Wu, Y. M., Zhao, L., Chen, H., Chen, Y. G., Chang, J. M., and Lin, C.
680 M.: A first near real-time seismology-based landquake monitoring system, *Sci. Rep.*,
681 7, 43510, <https://doi.org/10.1038/srep43510>, 2017.
- 682 Chen, C. H., Chao, W. A., Wu, Y. M., Zhao, L., Chen, Y. G., Ho, W. Y., Lin, T. L.,
683 Kuo, K. H., and Chang, J. M.: A seismological study of landquakes using a real-ti
684 me broad-band seismic network, *Geophys. J. Int.*, 194, 885-898, <http://doi.org/10.1093>
685 /gji/ggt121, 2013.
- 686 Dahlen, F. A.: Single-force representation of shallow landslide sources, *B. Seismol. Soc.*
687 *Am.*, 83, 130–143, <http://doi.org/10.1785/BSSA0830010130>, 1993.
- 688 Dammeier, F., Moore, J. R., Hammer, C., Haslinger, F., and Loew, S.: Automatic detecti
689 on of alpine rockslides in continuous seismic data using hidden Markov models, *J.*
690 *Geophys. Res.-Earth*, 121, 351-371, <http://doi.org/10.1002/2015jf003647>, 2016.
- 691 Darlington, W.J., Ranjith, P.G., and Choi, S.K.: The Effect of Specimen Size on Strength
692 and Other Properties in Laboratory Testing of Rock and Rock-Like Cementitious Br

693 little Materials, *Rock Mech Rock Eng*, 44, 513, <https://doi.org/10.1007/s00603-011-016>
694 1-6, 2011.

695 Deng, J. J., Gao, Y. J., Yu, Z. Q., and Xie, H. P.: Analysis on the Formation Mechanis
696 m and Process of Baige Landslides Damming the Upper Reach of Jinsha River, Chin
697 a, *Adv. Eng. Sci.*, 51, 9-16, <http://doi.org/10.15961/j.jsuese.201801438>, 2019.(In Chine
698 se)

699 Ekström, G., and Stark, C. P.: Simple scaling of catastrophic landslide dynamics, *Science*.
700 339, 1416–1419. <https://doi.org/10.1126/science.1232887>, 2013.

701 Fan, X., Yang, F., Subramanian, S. S., Xu, Q., Feng, Z., Mavrouli, O., Peng, M., Ouyan
702 g, C., Jansen, D., and Huang, R.: Prediction of a multi-hazard chain by an integrate
703 d numerical simulation approach: the Baige landslide, Jinsha River, China, *Landslide*
704 s, 17, 147-164, <http://doi.org/10.1007/s10346-019-01313-5>, 2019a.

705 Fan, X., Xu, Q., Liu, J., Subramanian, S. S., He, C., Zhu, X., and Zhou, L.: Successful
706 early warning and emergency response of a disastrous rockslide in Guizhou province,
707 China, *Landslides*, 16, 2445–2457, <https://doi.org/10.1007/s10346-019-01269-6>, 2019b.

708 Favreau, P., Mangeney, A., Lucas, A., Crosta, G., and Bouchut, F.: Numerical modeling
709 of landquakes, *Geophys. Res. Lett.*, 37, L15305, <http://doi.org/10.1029/2010gl043512>,
710 2010.

711 Feng, Z.: The seismic signatures of the 2009 Shiaolin landslide in Taiwan, *Nat. Hazards*
712 *Earth Syst. Sci.*, 11, 1559-1569, <http://doi.org/10.5194/nhess-11-1559-2011>, 2011.

713 Feng, Z. Y., Lo, C. M., and Lin, Q. F.: The characteristics of the seismic signals induce
714 d by landslides using a coupling of discrete element and finite difference methods,
715 *Landslides*, 14, 661-674, <http://doi.org/10.1007/s10346-016-0714-6>, 2016.

716 Froude, M. J., and Petley, D. N.: Global fatal landslide occurrence from 2004 to 2016,
717 *Nat. Hazards Earth Syst. Sci.*, 18, 2161-2181, <http://doi.org/10.5194/nhess-18-2161-201>
718 8, 2018.

719 Fuchs, F., Lenhardt, W., and Bokelmann, G.: Seismic detection of rockslides at regional
720 scale: examples from the Eastern Alps and feasibility of kurtosis-based event locatio
721 n, *Earth Surf. Dynam.*, 6, 955-970, <http://doi.org/10.5194/esurf-6-955-2018>, 2018.

722 Fukao, Y.: Single-force representation of earthquakes due to landslides or the collapse of
723 caverns, *Geophys. J. Int.*, 122, 243–248, <https://doi.org/10.1111/j.1365-246X.1995.tb03>
724 551.x, 1995.

725 Gualtieri, L., and Ekström, G.: Broad-band seismic analysis and modeling of the 2015 T
726 aan Fjord, Alaska landslide using Instaseis, *Geophys. J. Int.*, 213, 1912–1923, <https://>
727 doi.org/10.1093/gji/ggy086, 2018.

728 Hasegawa, H. S., and Kanamori, H.: Source mechanism of the magnitude 7.2 Grand Ban
729 ks earthquake of November 1929: Double couple or submarine landslide?, *B. Seismo*
730 *l. Soc. Am.*, 77, 1984–2004, 1987.

731 Helmstetter, A., and Garambois, S.: Seismic monitoring of Séchilienne rockslide (French
732 Alps): Analysis of seismic signals and their correlation with rainfall, *J. Geophys. Re*
733 *s.*, 115, F03016, <http://doi.org/10.1029/2009jf001532>, 2010.

734 Hencher, S. R., Richards, L. R.: Assessing the Shear Strength of Rock Discontinuities at
735 Laboratory and Field Scales, *Rock Mech Rock Eng*, 48, 883-905, [https://doi.org/10.1](https://doi.org/10.1007/s00603-014-0633-6)
736 007/s00603-014-0633-6, 2014.

737 Hibert, C., Ekström, G., and Stark, C. P.: Dynamics of the Bingham Canyon Mine lands
738 lides from seismic signal analysis, *Geophys. Res. Lett.*, 41, 4535–4541, [https://doi.org](https://doi.org/10.1002/2014GL060592)
739 /10.1002/2014GL060592, 2014.

740 Hibert, C., Stark, C. P., and Ekström, G.: Dynamics of the Oso-Steelhead landslide from
741 broadband seismic analysis, *Nat. Hazards Earth Syst. Sci.*, 15, 1265–1273, [https://doi.](https://doi.org/10.5194/nhess-15-1265-2015)
742 org/10.5194/nhess-15-1265-2015, 2015.

743 Hoek E.: Rock engineering course notes by Evert Hoek. [http://www.rocscience.com/educat](http://www.rocscience.com/education/hoek_corner)
744 ion/hoek_corner, 2000.

745 Jiang, Y., Wang, G., and Kamai, T.: Fast shear behavior of granular materials in ring-sh
746 ear tests and implications for rapid landslides, *Acta Geotech.*, 12, 645-655, [http://doi.](http://doi.org/10.1007/s11440-016-0508-y)
747 org/10.1007/s11440-016-0508-y, 2016.

748 Kääh, A., Leinss, S., Gilbert, A., Bühler, Y., Gascoin, S., Evans, S. G., Bartelt, P., Bert
749 hier, E., Brun, F., Chao, W. A., Farinotti, D., Gimbert, F., Guo, W., Huggel, C., Ka
750 rgel, J.S., Leonard, G.J., Tian, L., Treichler, D., and Yao, T.: Massive collapse of t
751 wo glaciers in western Tibet in 2016 after surge-like instability, *Nat. Geosci.*, 11, 11
752 4–120, <https://doi.org/10.1038/s41561-017-0039-7>, 2018.

753 Kanamori, H., and Given, J.W.: Analysis of long-period seismic waves excited by the M
754 ay 18, 1980, eruption of Mount St. Helens—A terrestrial monopole?, *J. Geophys. Re*
755 s.-Sol. Ea., 87, 5422–5432, <https://doi.org/10.1029/JB087iB07p05422>, 1982.

756 Kanamori, H., Given, J. W., and Lay, T.: Analysis of seismic body waves excited by th
757 e Mount St. Helens eruption of May 18, 1980, *J. Geophys. Res.-Sol. Ea.*, 89, 1856–
758 1866, <https://doi.org/10.1029/JB089iB03p01856>, 1984.

759 Kao, H., Kan, C. W., Chen, R. Y., Chang, C. H., Rosenberger, A., Shin, T .C., Leu, P.
760 L., Kuo, K. W., and Liang, W. T.: Locating, monitoring, and characterizing typhoon
761 -induced landslides with real-time seismic signals, *Landslides*, 9, 557-563, [http://doi.o](http://doi.org/10.1007/s10346-012-0322-z)
762 rg/10.1007/s10346-012-0322-z, 2012.

763 Li, C. Y., Wang, X. C., He, C. Z., Wu, X., Kong, Z. Y., and Li, X. L. China National
764 Digital Geological Map (Public Version at 1:200 000 Scale) Spatial Database(V1). D
765 evelopment and Research Center of China Geological Survey; China Geological Surv
766 ey[producer], 1957. National Geological Archives of China [distributor], 2019-06-30.
767 <https://doi.org/10.23650/data.A.2019.NGA120157.K1.1.1.V1>, 2019a.

768 Li, W., Chen, Y., Liu, F., Yang, H., Liu, J., and Fu, B.: Chain-style landslide hazardous
769 process: Constraints from seismic signals analysis of the 2017 Xinmo landslide, SW
770 China, *J. Geophys. Res.-Sol. Ea.*, 124, 2025–2037, [https://doi.org/10.1029/2018JB0164](https://doi.org/10.1029/2018JB016433)
771 33, 2019b.

772 Li, Z., Huang, X., Xu, Q., Yu, D., Fan, J., and Qiao, X.: Dynamics of the Wulong land
773 slide revealed by broadband seismic records, *Earth, Planets Space*, 69, 27, [https://doi.](https://doi.org/10.1186/s40623-017-0610-x)
774 org/10.1186/s40623-017-0610-x, 2017.

775 Li, Z., Huang, X., Yu, D., Su, J., and Xu, Q.: Broadband-seismic analysis of a massive
776 landslide in southwestern China: Dynamics and fragmentation implications, *Geomorph*
777 *ology*, 336, 31–39. <https://doi.org/10.1016/j.geomorph.2019.03.024>, 2019c.

778 Liu, C., Pollard, D. D., and Shi, B.: Analytical solutions and numerical tests of elastic a
779 nd failure behaviors of close-packed lattice for brittle rocks and crystals, *J. Geophys.*
780 *Res.-Sol. Ea.*, 118, 71-82, <https://doi.org/10.1029/2012JB009615>, 2013.

781 Liu, C., Xu, Q., Shi, B., Deng, S., and Zhu, H.: Mechanical properties and energy conve
782 rsion of 3D close-packed lattice model for brittle rocks, *Comput. Geosci.*, 103, 12-20,
783 <https://doi.org/10.1016/j.cageo.2017.03.00>, 2017.

784 Liu, C., Fan, X., Zhu, C., and Shi, B.: Discrete element modeling and simulation of 3-D
785 imensional large-scale landslide-Taking Xinmocun landslide as an example, *J. Eng. G*
786 *eol*, 27, 1362-1370, <https://doi.org/10.13544/j.cnki.jeg.2018-234>, 2019. (In Chinese)

787 Lo, C. M., Lin, M. L., Tang, C. L., and Hu, J. C.: A kinematic model of the Hsiaolin
788 landslide calibrated to the morphology of the landslide deposit, *Eng. Geol.*, 123, 22-
789 39, <https://doi.org/10.1016/j.enggeo.2011.07.002>, 2011.

790 McNamara, D.E., Buland, R.P., 2004. Ambient Noise Levels in the Continental United St
791 ates. *Bull. Seismol. Soc. Am.* 94, 1517–1527. <https://doi.org/10.1785/012003001>

792 Mergili, M., Fischer, J. T., Krenn, J., and Pudasaini, S. P.: r. avaflow v1, an advanced o
793 pen-source computational framework for the propagation and interaction of two-phase
794 mass flows, *Geosci. Model Dev*, 10, 553-569, [https://doi.org/10.5194/gmd-10-553-201](https://doi.org/10.5194/gmd-10-553-2017)
795 7, 2017.

796 Mergili, M., Emmer, A., Juřicová A., Cochachin, A., Fischer, J. T., Huggel, C., and Pud
797 asaini, S. P.: How well can we simulate complex hydro-geomorphic process chains?
798 The 2012 multi-lake outburst flood in the Santa Cruz Valley (Cordillera Blanca, Per
799 ú), *Earth Surf Process Landf*, 43, 1373-1389, <https://doi.org/10.1002/esp.4318>, 2017.

800 Moore, J. R., Pankow, K. L., Ford, S. R., Koper, K. D., Hale, J. M., Aaron, J., and Lar
801 sen, C.F.: Dynamics of the Bingham Canyon rock avalanches (Utah, USA) resolved
802 from topographic, seismic, and infrasound data, *J. Geophys. Res.-Earth*, 122, 615–64
803 0, <https://doi.org/10.1002/2016JF004036>, 2017.

804 Moretti, L., Mangeney, A., Capdeville, Y., Stutzmann, E., Huggel, C., Schneider, D., and
805 Bouchut, F.: Numerical modeling of the Mount Steller landslide flow history and of
806 the generated long period seismic waves, *Geophys. Res. Lett.*, 39, L16402, [https://do](https://doi.org/10.1029/2012GL052511)
807 [i.org/10.1029/2012GL052511](https://doi.org/10.1029/2012GL052511), 2012.

808 Moretti, L., Allstadt, K., Mangeney, A., Capdeville, Y., Stutzmann, E., and Bouchut, F.:
809 Numerical modeling of the Mount Meager landslide constrained by its force history
810 derived from seismic data, *J. Geophys. Res.-Sol. Ea.*, 120, 2579–2599, [https://doi.org/](https://doi.org/10.1002/2014JB011426)
811 [10.1002/2014JB011426](https://doi.org/10.1002/2014JB011426), 2015.

812 Muceku, Y., Korini, O., and Kuriqi, A.: Geotechnical analysis of hill’s slopes areas in h
813 eritage town of Berati, Albania. *Period. Polytech., Civ. Eng.* 60, 61-73, [https://doi.org/](https://doi.org/10.3311/PPci.7752)
814 [10.3311/PPci.7752](https://doi.org/10.3311/PPci.7752), 2016.

815 Ouyang, C. J., An, H. C., Zhou, S., Wang, Z. W., Su, P. C., and Wang, D. P.: Insights
816 from the failure and dynamic characteristics of two sequential landslides at Baige v
817 illage along the Jinsha River, China, *Landslides*, 16, 1397-1414, [https://doi.org/10.1007](https://doi.org/10.1007/s10346-019-01177-9)
818 /s10346-019-01177-9, 2019.

819 Pastor, M., Blanc, T., Haddad, B., Petrone, S., Sanchez, M. M., Drempevic, V., Issler, D.,
820 Crosta, G. B., Cascini, L., Sorbino, G., and Cuomo, S.: Application of a SPH dept
821 hintegated model to landslide run-out analysis, *Landslides*, 11, 793812, [https://doi.or](https://doi.org/10.1007/s10346-014-0484-y)
822 g/10.1007/s10346-014-0484-y, 2014.

823 Peterson, J.R., 1993. Observations and modeling of seismic background noise, U.S. Geolo
824 gical Survey Open-File Report 93-322. <https://doi.org/10.3133/ofr93322>.

825 Pitman, E. B., Nichita, C. C., Patra, A., Bauer, A., Sheridan, M., and Bursik, M.: Comp
826 uting granular avalanches and landslides, *Phys. Fluids.*, 15, 3638-3646, [https://doi.org/](https://doi.org/10.1063/1.1614253)
827 10.1063/1.1614253, 2003.

828 Sakals, M. E., Geertsema, M., Schwab, J. W., and Foord, V. N.: The Todagin Creek lan
829 dslide of October 3, 2006, Northwest British Columbia, Canada, *Landslides*, 9, 107-1
830 15, <http://doi.org/10.1007/s10346-011-0273-9>, 2011.

831 Schöpa, A., Chao, W. A., Lipovsky, B. P., Hovius, N., White, R. S., Green, R. G., and
832 Turowski, J. M.: Dynamics of the Askja caldera July 2014 landslide, Iceland, from
833 seismic signal analysis: precursor, motion and aftermath, *Earth Surf. Dynam.*, 6, 467
834 -485, <https://doi.org/10.5194/esurf-6-467-2018>, 2018.

835 Shen, W., Li, T., Li, P., and Lei, Y.: Numerical assessment for the efficiencies of check
836 dams in debris flow gullies: A case study, *Comput. Geotech.*, 122, 103541, [https://doi.](https://doi.org/10.1016/j.compgeo.2020.103541)
837 org/10.1016/j.compgeo.2020.103541, 2020.

838 Sheng, M., Chu, R., Wang, Y., and Wang, Q.: Inversion of source mechanisms for singl
839 e-force events using broadband waveforms, *Seismol. Res. Lett.*, 91, 1820-1830, <https://doi.org/10.1785/0220190349>, 2020.

841 Soga, K., Alonso, E., Yerro, A., Kumar, K., and Bandara, S.: Trends in large-deformatio
842 n analysis of landslide mass movements with particular emphasis on the material poi
843 nt method, *Géotechnique*, 66, 1-26, <https://doi.org/10.1680/jgeot.15.lm.005>, 2016.

844 Walter, M., Arnhardt, C., and Joswig, M.: Seismic monitoring of rockfalls, slide quakes,
845 and fissure development at the Super-Sauze mudslide, French Alps, *Eng. Geol.*, 128,
846 12-22, <http://doi.org/10.1016/j.enggeo.2011.11.002>, 2012.

847 Wang, L. Q., Yin, Y. P., Huang, B. L., and Dai, Z. W.: Damage evolution and stability
848 analysis of the Jianchuandong Dangerous Rock Mass in the Three Gorges Reservoir
849 Area, *Eng. Geol.*, 265, 105439, <http://dx.doi.org/10.1016/j.enggeo.2019.105439>, 2020a.

850 Wang, L., Wu, C. Z., Gu, X., Liu, H. L., Mei, G. X., and Zhang, W. G.: Probabilistic
851 stability analysis of earth dam slope under transient seepage using multivariate adapti
852 ve regression splines, *Bull. Eng. Geol. Environ.*, 79, 2763-2775, [http://dx.doi.org/10.1](http://dx.doi.org/10.1007/s10064-020-01730-0)
853 007/s10064-020-01730-0, 2020b.

854 Wang, R.: A simple orthonormalization method for stable and efficient computation of G
855 reen's functions, *B. Seismol. Soc. Am.*, 89, 733-741, 1999.

856 Wang, W., Yin, Y., Zhu, S., Wang, L., Zhang, N., and Zhao, R.: Investigation and numerical modeling of the overloading-induced catastrophic rockslide avalanche in Baige, 857
 858 Tibet, China, *Bull. Eng. Geol. Environ.*, 79, 1765-1779, [https://doi.org/10.1007/s10064](https://doi.org/10.1007/s10064-019-01664-2)
 859 -019-01664-2, 2020c.

860 Wang, Y. F., Dong, J. J., Cheng, Q. G.: Velocity-dependent frictional weakening of large 861
 862 rock avalanche basal facies: Implications for rock avalanche hypermobility?, *J. Geophys. Res.-Sol. Ea.*, 122, 1648-1676, <https://doi.org/10.1002/2016JB013624>, 2017.

863 Wang, Y. F., Dong, J. J., Cheng, Q. G.: Normal stress-dependent frictional weakening of 864
 865 large rock avalanche basal facies: Implications for the rock avalanche volume effect, *J. Geophys. Res.-Sol. Ea.*, 123, 3270-3282, <https://doi.org/10.1002/2018JB015602>, 2
 866 018.

867 Xu, Q., Zheng, G., Li, W. L., He, C. Y., Dong, X. J., Guo, C., and Feng, W. K.: Study 868
 869 on Successive Landslide Damming Events of Jinsha River in Baige Village on October 11 and November 3, 2018, *J. Eng. Geo*, 26, 1534-1551, <https://doi.org/10.13544/j.cnki.jeg.2018-406>, 2018. (In Chinese)

871 Yamada, M., Matsushi, Y., Chigira, M., Mori, J.: Seismic recordings of landslides caused 872
 873 by Typhoon Talas (2011), Japan, *Geophys. Res. Lett.*, 39, L13301, <http://doi.org/10.1029/2012gl052174>, 2012.

874 Yamada, M., Kumagai, H., Matsushi, Y., and Matsuzawa, T.: Dynamic landslide processes 875
 876 revealed by broadband seismic records, *Geophys. Res. Lett.*, 40, 2998-3002, <https://doi.org/10.1002/grl.50437>, 2013.

877 Yamada, M., Mangeney, A., Matsushi, Y., and Moretti, L.: Estimation of dynamic friction 878
 879 of the Akatani landslide from seismic waveform inversion and numerical simulation, *Geophys. J. Int.*, 206, 1479-1486. <https://doi.org/10.1093/gji/ggw216>, 2016.

880 Yamada, M., Mangeney, A., Matsushi, Y., and Matsuzawa, T.: Estimation of dynamic friction 881
 882 and movement history of large landslides, *Landslides*, 15, 1963-1974, <https://doi.org/10.1007/s10346-018-1002-4>, 2018.

883 Yan, Y., Cui, P., Chen, S., Chen, X., Chen, H., and Chien, Y.: Characteristics and interpretation 884
 885 of the seismic signal of a field-scale landslide dam failure experiment, *J. Mt. Sci.*, 14(2): 219-236. <https://doi.org/10.1007/s11629-016-4103-3>, 2017.

886 Yan, Y., Cui, Y., Guo, J., Hu, S., Wang, Z., and Yin, S.: Landslide reconstruction using 887
 888 seismic signal characteristics and numerical simulations: Case study of the 2017 “6.24” Xinmo landslide, *Eng. Geol.*, 270, 105582, <http://doi.org/10.1016/j.enggeo.2020.105582>, 2020a.

890 Yan, Y., Cui, Y., Tian, X., Hu, S., Guo, J., Wang, Z., Yin, S., and Liao, L.: Seismic signal 891
 892 recognition and interpretation of the 2019 “7.23” Shuicheng landslide by seismogram stations, *Landslides*, 17, 1191-1206, <http://doi.org/10.1007/s10346-020-01358-x>, 2
 893 020b.

894 Yu, D., Huang, X., and Li, Z.: Variation patterns of landslide basal friction revealed from 895
 896 long-period seismic waveform inversion, *Nat. Hazards*, 100, 313-327, <https://doi.org/10.1007/s11069-019-03813-y>, 2020.

897 Zhang, L., Xiao, T., He, J., and Chen, C.: Erosion-based analysis of breaching of Baige
898 landslide dams on the Jinsha River, China, in 2018, *Landslides*, 16, 1965-1979, [http](http://doi.org/10.1007/s10346-019-01247-y)
899 [s://doi.org/10.1007/s10346-019-01247-y](http://doi.org/10.1007/s10346-019-01247-y), 2019.

900 Zhang, S. L., Yin, Y. P., Hu, X. W., Wang, W. P., Zhang, N., Zhu, S. N., and Wang,
901 L. Q.: Dynamics and emplacement mechanisms of the successive Baige landslides on
902 the Upper Reaches of the Jinsha River, China, *Eng. Geol.*, 278, 105819, [http://dx.d](http://dx.doi.org/10.1016/j.enggeo.2020.105819)
903 [oi.org/10.1016/j.enggeo.2020.105819](http://dx.doi.org/10.1016/j.enggeo.2020.105819), 2020a.

904 Zhang, Z., He, S., Liu, W., Liang, H., Yan, S., Deng, Y., Bai, X., and Chen, Z.: Source
905 characteristics and dynamics of the October 2018 Baige landslide revealed by broad
906 band seismograms, *Landslides*, 16, 777-785, <http://doi.org/10.1007/s10346-019-01145-3>,
907 2019.

908 Zhang, Z., He, S., and Li, Q.: Analyzing high-frequency seismic signals generated during
909 a landslide using source discrepancies between two landslides, *Eng. Geol.*, 272, 105
910 640, <https://doi.org/10.1016/j.enggeo.2020.105640>, 2020b.

911 Zhao, J., Moretti, L., Mangeney, A., Stutzmann, E., Kanamori, H., Capdeville, Y., Calder,
912 E. S., Hibert, C., Smith, P. J., Cole, P., and Lefriant, A.: Model space exploration
913 for determining landslide source history from long-period seismic data, *Pure Appl. G*
914 *eophys.*, 172, 389–413, <https://doi.org/10.1007/s00024-014-0852-5>, 2015.

915 Zhao, J., Ouyang, C. J., Ni, S. D., Chu, R. S., and Mangeney, A.: Analysis of the 2017
916 June Maoxian landslide processes with force histories from seismological inversion
917 and terrain features, *Geophys. J. Int.*, 222, 1965–1976, <https://doi.org/10.1093/gji/ggaa>
918 226, 2020.

919 Zhou, L., Fan, X., Xu, Q., Yang, F., and Gou, C.: Numerical simulation and hazard pre
920 diction on movement process characteristics of Baige landslide in Jinsha river, *Eng.*
921 *Geol.*, 27, 1395-1404, <https://doi.org/10.13544/j.cnki.jeg.2019-037>, 2019.(In Chinese)